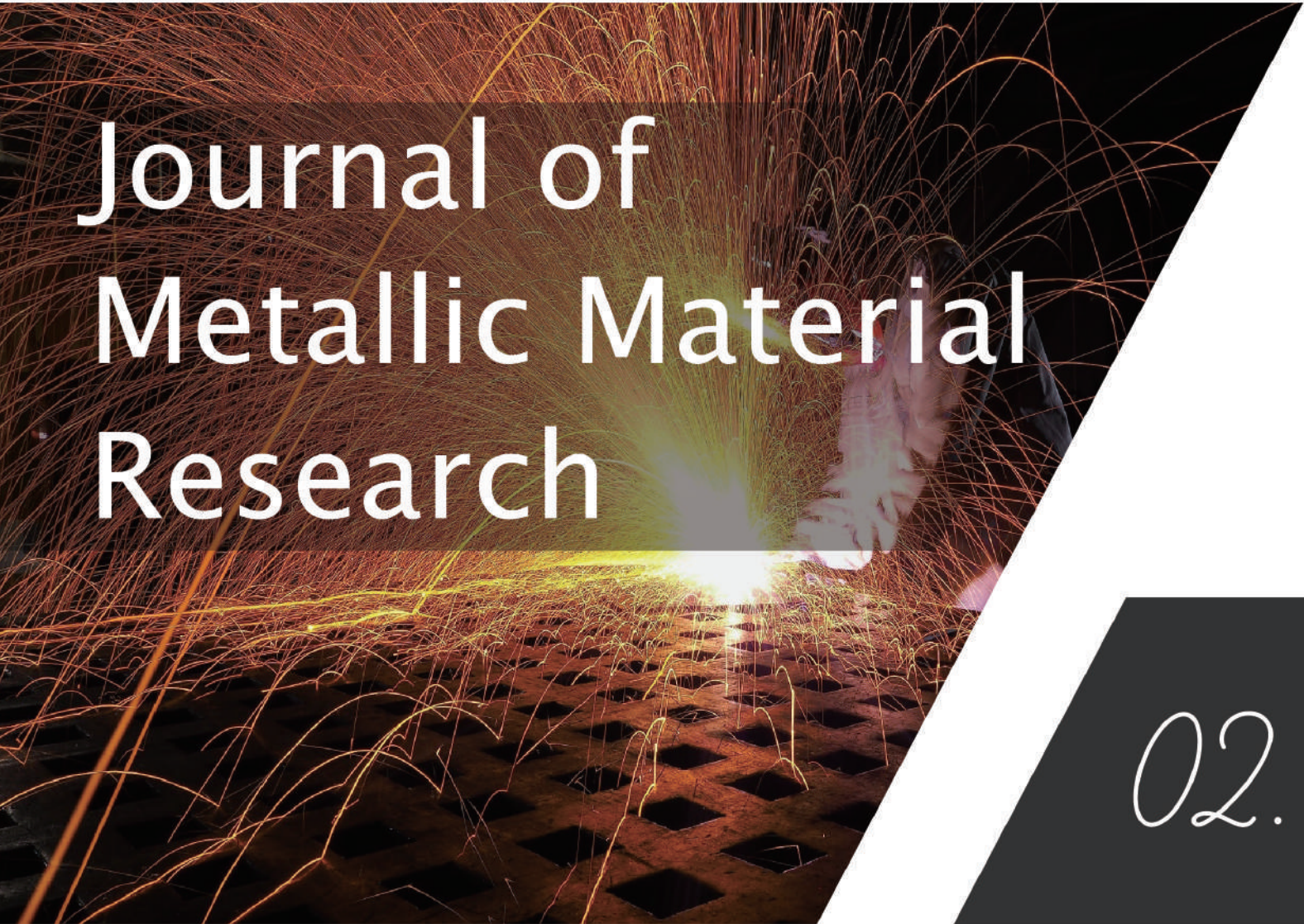




**BILINGUAL
PUBLISHING CO.**
Pioneer of Global Academics Since 1984

2019 October



Journal of Metallic Material Research

02.

October Volume 2 Issue 2 ISSN 2630-5135 (Online)

Editor-in-Chief

Dr. Oleg Valentinovich

Sobol, Ukraine

Editorial Board Members

- | | |
|---|--|
| Shuo Chen, United States | Alexander Evgenievich Barmin, Ukraine |
| Changrui Wang, China | Khitam Abdulhussein Saeed, Malaysia |
| Recep Karadag, Turkey | Sertan Ozan, Turkey |
| Madhukar Eknath Navgire, India | Anand Krishnan, South Africa |
| Unal Camdali, Turkey | Farshad Darab-Golestan, Iran |
| Jitendra Kumar Singh, Korea | Mohammadreza Elahifard, Iran |
| Abhay Nanda Srivastva, India | Paparao Mondri, India |
| Vivek Patel, India | Zbigniew Ranachowski, Poland |
| Aybaba Hançerlloğullari, Turkey | Sami ullah Rather, Saudi Arabia |
| Bandar Abdulaziz AlMangour, Saudi Arabia | Nickolaj Nikolayevich Rulyov, Ukraine |
| Soumen Maiti, India | Oğuzhan Keleştemur, Turkey |
| Jonathan David Parker, Canada | Shengqiang Ma, China |
| Jingyuan Yan, United States | Md Saiful Islam, Bangladesh |
| Satyanarayana Sirasani, India | Ajay Kumar Choubey, India |
| Xiaohan Hu, China | Saeed Kakaei, Iran |
| Derya Dispinar, Turkey | Hojat Jafari, Iran |
| Samson jerold samuel Chelladurai, India | Yuhan Liang, United States |
| Akash Deep Sharma, India | Ahmed Wagih, Egypt |
| Dan Dobrotă, Romania | Bhanodaya Kiran Babu Nadikudi, India |
| Asit Kumar Gain, Australia | Rong Liu, Canada |
| Dragica Milan Minic, Serbia | Mahmoud Pakshir, Iran |
| Zabiollah Mahdaviyar, Iran | Changhai Zhou, China |
| Chandan Pandey, India | Vishal Ishvarbhai Lad, United States |
| Mahnaz Mahdavi Shahri, Iran | Hossein Ghasemi Mobtaker, Iran |
| Janarathanan Gopalakrishnan, India | Francesco Caridi, Italy |
| Deniz Uçar, Turkey | Konstanti Viktorovich Ivanov, Russian Federation |
| Weidong Song, China | Dipak Kumar, India |
| Attoui Aissa, Algeria | Americo Scotti, Brazil |
| Mohammad Farnush, Iran | Ziad Salem Abu-Hamatteh, Jordan |
| Qiaoli Lin, China | Mohsen Vafaeifard, Malaysia |
| Hajar Zarei Se Dehi Zadeh, Iran | Hülya - Demirören, Turkey |
| Subravel Visvalingam, India | Tahir Mohiuddin Bhat, India |
| Asaminew Abiyu Cherinet, Ethiopia | Hamit Özkan Gülsoy, Turkey |
| Arif Gök, Turkey | Sandhya Dwevedi, India |
| Ning Li, China | Sergey Nikolaevich Lezhnev, Kazakhstan |
| Fufa Wu, China | Faysal Fayez Eliyan, Canada |
| Wenchun Jiang, China | Shouxun Ji, United Kingdom |
| Saeed Zeinali Heris, Iran | Patrice Berthod, France |
| Himadri Bhusan Sahoo, India | Moslem Mansour Lakouraj, Iran |
| Vladimir Victorovich Lukov, Russian Federation | Akhyar - Akhyar, Indonesia |
| Abhishek Ghosh, India | Chih-Chun Hsieh, Taiwan |
| KangHua Chen, China | Recep Sadeler, Turkey |
| Pradeep L Menezes, United States | Lutfiddin Omanivich Olimov, Uzbekistan |
| Shuhua Zhang, China | Mahmoud Ebrahimi, Iran |
| Naushad Ahmad, India | Lineker Max Goulart Coelho, Brazil |
| S Selvam, India | Aslihan Katip, Turkey |
| Guocheng Zhu, China | Serkan ISlak, Turkey |
| Mohamed Kamal ElFawkhry, India | Murat Sarikaya, Turkey |
| Mohammad Hassan Shirani Bidabadi, China | Yaofeng Chang, United States |
| Mohd Azli Salim, Malaysia | Mehmet Kaya, Turkey |
| Vladimir Mikhailov Yegorovich, Russian Federation | Yahya Absalan, Russian Federation |
| Kaveh Sheikhi Moghaddam, Iran | Xiang Wang, China |
| Robin Gupta, India | Meilinda Nurbanasari, Indonesia |
| Sergey Vasilevich Byvaltsev, Russian Federation | Rizk Mostafa Shalaby, Egypt |
| Nitin Saini, India | Anatolii Michailovich Lepikhin, Russian Federation |
| Ramesh Balakrishnan, India | |

Volume 2 Issue 2 • October 2019 • ISSN 2630-5135 (Online)

Journal of Metallic Material Research

Editor-in-Chief

Dr. Oleg Valentinovich



**BILINGUAL
PUBLISHING CO.**

Pioneer of Global Academics Since 1984

Contents

Article

- 1 Stereological Evaluation of Precipitates within Ferrite Grains in Heat-Treated 1.25Cr0.5-Mo Steel Previously Exposed to Service**
Rafael Fernández-Fuentes Americo Scotti Amado Cruz-Crespo Roberto Silva González
Rafael Ariza Nelson Guedes de Alcantara
- 15 Behaviour of Friction Stir Dissimilar Welded Blanks and The Role of Different Tool Pin Profiles**
Bhanodaya Kiran Babu Nadikudi
- 20 Study on the Crystal Structure and Microstructure Evolution of Shock-processed Titanium Powder**
A.D. Sharma A.K. Sharma N.Thakur

Review

- 9 Synthesis, Characterization and Applications of MoO_3 - Fe_3O_4 Nanocomposite Material**
Madhukar Navgire Akash Nagare Ganesh Kale Sandesh Bhitre

Copyright

Journal of Metallic Material Research is licensed under a Creative Commons-Non-Commercial 4.0 International Copyright (CC BY- NC4.0). Readers shall have the right to copy and distribute articles in this journal in any form in any medium, and may also modify, convert or create on the basis of articles. In sharing and using articles in this journal, the user must indicate the author and source, and mark the changes made in articles. Copyright © BILINGUAL PUBLISHING CO. All Rights Reserved.



ARTICLE

Stereological Evaluation of Precipitates within Ferrite Grains in Heat-Treated 1.25Cr0.5Mo Steel Previously Exposed to Service

Rafael Fernández-Fuentes¹ Americo Scotti^{2,4*} Amado Cruz-Crespo¹ Roberto Silva González¹ Rafael Ariza² Nelson Guedes de Alcantara³

1. Universidad Central Marta Abreu de Las Villas – UCLV, Cuba
2. Universidade Federal de Uberlândia – UFU, Brazil
3. Universidade Federal de São Carlos – UFSCar, Brazil
4. University of West, Department of Engineering Science, Trollhättan, Sweden

ARTICLE INFO

Article history

Received: 12 July 2019

Accepted: 30 September 2019

Published Online: 30 October 2019

Keywords:

Creep-resistant 1.25Cr0.5Mo Steel

Repairing

PWHT

Precipitation coarsening

ABSTRACT

The objective of this work was to study the effect of the heat treatment and further operation aging on the stereological parameters (size, quantity and volume fraction) of precipitates within ferrite grains of a creep-resistant 1.25Cr0.5Mo steel after long-term operation. The heat treatment was similar to the treatment that is carried out in industrial steam pipelines after welding (post weld heat treatment - PWHT) during installation and/or repairing. The operation aging corresponds to a subsequent long in-service operation after repairing. To determine the stereological parameters, SEM digital images were taken from samples of this material after conditions of in-service-aged (after long-term operation), in-service-aged and heat-treated (simulating repairing) and in-service-aged, heat-treated and in-laboratory aged (simulating subsequent long-term operation after repairing). The results indicate that the changes in the stereological parameters of the precipitates within ferrite grains after PWHT is associated with the coarsening process of the within-ferrite-grain precipitates as well as stabilizing the microstructure, since the material aging after PWHT of an in-serviced aged material would not change the stereological parameters.

1. Introduction

In electric power generation and oil processing plants, several structural steel components are subjected to working conditions that undergo mechanical loads at temperatures between 450 and 600 °C. This is the case of the steam generators and the respective pipelines used for steam conduction. Under these working conditions, these components experience the phenomenon known as creep, which can lead to failure due to plastic deformation over

time and even breakage^[1]. To ensure safe and long-term use of these components, low-alloy Cr-Mo steels have been developed, among other materials^[2]. In these steels, the creep resistance is achieved by the action of two hardening mechanisms: solid solution and precipitation^[3].

To uncover the creep resistance of the component material, accelerated tests are applied to determine the stress level at which a certain temperature causes the rupture or 1% of plastic deformation after 10⁵ hours (11.4 years) by

**Corresponding Author:*

Americo Scotti,

Universidade Federal de Uberlândia – UFU, Brazil; University of West, Department of Engineering Science, Trollhättan, Sweden;

Email: americo.scotti@hv.se

means of the extrapolation. These accelerated tests use the Larson-Miller parameter (LMP), which represents the time and temperature equivalence for this type of steel under the thermally activated creep process of stress rupture. It permits the calculation of the equivalent times necessary for stress rupture to occur at different temperatures.^[4] However, in practice, it has been established that the useful life of the components manufactured with low alloy CrMo steel can reach and exceed 20 and even 30 years^[5]. Nevertheless, premature failures frequently arise in the components manufactured with these steels that are associated with the weld region susceptible to the formation of non-acceptable cracks^[6].

When these failures occur, and when it is technically-economically justified, repair is performed by removing the damaged section and welding an insert of a new material. The standards that are applied for this type of welding repair contemplate technological fabrication requirements to guarantee the quality of the welded joint of the new materials. However, the problem becomes complex in relation to the material exposed to service and which is thermally affected during the repair^[7]. The complexity of the subject is increased when the application of post-weld heat treatment (PWHT) after repairing is required. In this regards, divergences in literature on whether PWHT after repairing is favorable or not from the point of view of the residual life, is noticed^[7].

The PWHT is generally carried out in situ with localized heating, which imposes an additional thermal cycle on different regions of the weld (fusion – FZ - and heat-affected zones - HAZ) as well as the base metal that originally had not been exposed to the welding thermal cycle, as illustrated in Figure 1. Due to this localized heat treatment characteristic, it is not the whole component that undergoes the effect of the PWHT thermal cycle.

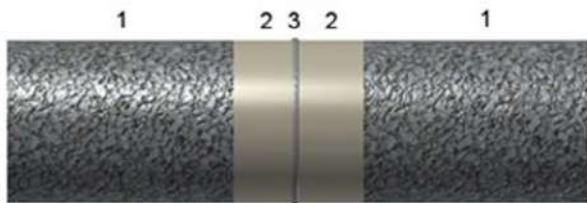


Figure 1. Schematization of the thermal affected zones associated with the localized (in situ) PWHT

Note: 1 - base metal not affected by the PWHT thermal cycle; 2 - zone of the base metal affected only by the PWHT thermal cycle; 3 - weld zone (fusion and HAZ) affected by both the welding and the PWHT thermal cycles.

The intrinsic complexity of the subject justifies the demand for further investigations on the effect of PWHT on

the performance of creep-resistant low alloy CrMo steels. For example, knowledge about micro-structural stability, aiming at establishing how the microstructure behaves in steels subjected to creep, turns out to be of great importance to have elements for decision-making during maintenance of these industrial components. However, concurrent metallurgical phenomena lead to the variation of the microstructure under the effect of temperature and time. Consequently, attention has been paid to the relationship between microstructure and the behavior of steel under creep^[8-11]. Among these phenomena, in the case of low alloy CrMo steels, spheroidization of perlite, graphitization, as well as precipitation, dissolution and growth of carbides stand out^[12]. There has been a marked interest in studying the phenomena specifically related to the evolution of precipitates^[2,13]. For this reason, the purpose of the present work is to study the influence of PWHT as part of a repairing procedure, just after repairing and after subsequent operation aging, on the stereological parameters (size, quantity and volume fraction) of precipitates within ferrite grains in 1.25Cr0.5Mo steel of a steam pipeline service-aged for more than 20 years at 480 °C.

2. Materials and Methods

For this study, a 150-mm-long segment of the base material (with no weld) was taken from a pipe section that was removed (during repair operation) from a 300-mm-diameter and 12-mm-thick wall steam pipeline. This material had been in operation for approximately 20 years at 480 °C. The determined chemical composition of the pipeline material (table 1) corresponds to that of an 1.25Cr0.5Mo steel, classified as A335 Grade P11, according to the ASTM A335 standard^[14]. Using the material of this pipe segment, this work was carried out with samples under three experimental conditions (figure 2). The first one, referred hereafter as ISA (in-service-aged material, as removed from the pipeline, to be used as reference). A second condition (dedicated to evaluate the effect of a PWHT) referred to the same material of the ISA condition, but after undergoing a heat treatment to simulate the PWHT that is carried out after repair operations (hereafter referred as ISA+PWHT). Therefore, the ISA+PWHT condition is a simulation of the in-service-aged material (ISA condition) that would be affected only by the PWHT, i.e., a material corresponding to the region located between the weld affected zone and the base metal (section 2 of Figure 1). The heat treatment to simulate the PWHT was performed in a furnace, at a heating speed of 200 °C h⁻¹ and keeping a soaking time of 1.5 h at 700 °C, in accordance with the recommendations of section VIII - division 1 of the ASME standard^[15].

Table 1. Determined chemical composition of the pipeline material

C	Si	Mn	P	S	Cr	Mo	W	Ti	V
0.12	0.18	0.41	≤0.03	≤0.03	1.24	0.49	≤0.01	≤0.01	≤0.01

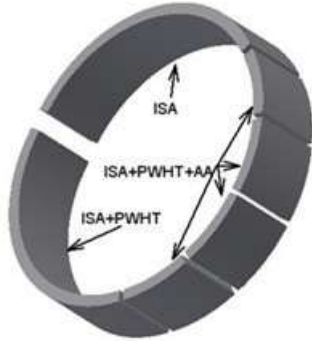


Figure 2. Sampling schematization of the pipe segment

Note: Corresponding to the studied experimental conditions, where ISA means the original material after in-service-aging, ISA+PWHT the original aged material to undergo heat treatment to simulate the PWHT and ISA+PWHT+AA the original aged and heat treated material to undergo accelerated thermal aging treatments.

Finally, a third condition (planned to evaluate the in-service thermal stability of the microstructure after the repair and PWHT) referred to the same material of the ISA+PWHT condition, but after undergoing accelerated thermal aging treatments (hereafter referred to as ISA+PWHT+AA). Four slices were removed for representing this latter condition (hereafter referred to as ISA+PWHT+AA-1, ISA+PWHT+AA-2, ISA+PWHT+AA-3 and ISA+PWHT+AA-4), aiming at different equivalent times during aging treatments. The aging parameters were selected so that they encompass ranges of temperature and time that would allow values of the Larson-Miller parameter (LMP) equivalent to times between 20000 and 100000 h at the service temperature (table 2). Therefore, the accelerated thermal aging treatments in this work was carried out using the same thermal cycle of a creep test, however without load application on the material.

Table 2. Time (t) and temperature (T) values for accelerated aging, Larson-Miller parameter (LMP) and equivalent time at the service temperature (teq).

Samples	T (°C)	t (h)	LMP=T(18 + log t)	teq (h)
ISA+PWHT+AA -1	550	1120	17325	101616
ISA+PWHT+AA -2	575	95	16830	22776
ISA+PWHT+AA -3	550	510	17042	42924
ISA+PWHT+AA -4	600	18	16810	21024

Specimens (10 mm x 10 mm x 10 mm) for Scanning

Electron Microscopy (SEM) were taken from the steam pipeline material representing each experimental condition. They were prepared by grinding and polishing to a 1µm finish, according to ASTM E3-11 [16], and etching with 1 % NITAL, in accordance with ASTM E407-11 [17]. SEM digital images of 3072 x 2304 pixels and resolution of 10 nm/pixel were obtained. Using 10 images from each condition and a digital image processing software, micrograph processing was performed and the amount of precipitates per unit area (NA) was counted. In addition, the equivalent 2D diameter (Di), which depends on the area occupied by each section of precipitate in the image and on the volume fraction (Vv), according with the fraction of the area (AA), were assessed.

From the particle sizes (Di), the relative frequency histograms were made (using in all cases 15 classes of size equal to 0.04 µm and more than 2500 measured particles) and the probability density was determined in each class interval, which is calculated by dividing the number of counts for each size class of the observed distribution by the total number (N) of analyzed particles and the class width (ΔD) [18]. The experimental values of the probability density were adjusted to a lognormal probability density function with two parameters (equation 1) and the parameters of the distribution function were obtained according to [19]. So as to establish the quality of the adjustment, the coefficient of determination (c.o.d) and "test F" were used in the analysis of variance [20, 21].

$$f_{LN}(D_i; D_g, \sigma_g) = \frac{1}{D_i \sqrt{2\pi \ln \sigma_g}} \exp \left[-\frac{1}{2} \left(\frac{\ln(D_i/D_g)}{\ln \sigma_g} \right)^2 \right] \quad (1)$$

where:

- Di – equivalent 2D diameter, (µm)
- Dg – geometric mean diameter, (µm)
- σg – geometric standard deviation

From the 2D stereological parameters, the 3D parameters were determined: average diameter (Dv) and number of particles per unit volume (Nv), these two parameters are determined by the expressions (2) and (3) respectively [18].

$$\overline{D}_V = \frac{\pi N}{2} \left[\sum_{i=1}^N \frac{1}{D_i} \right]^{-1} \quad (2)$$

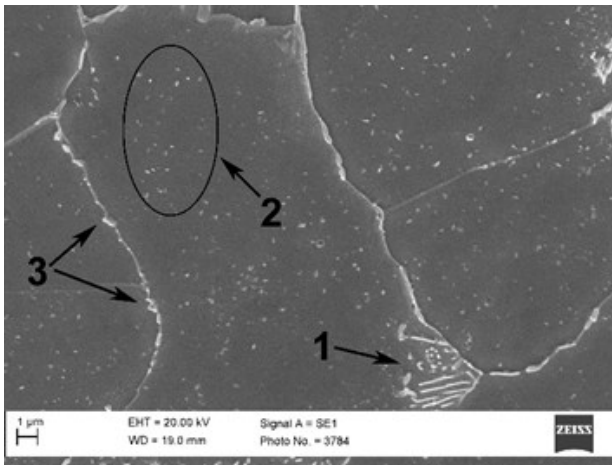
$$N_V = \frac{N_A}{\overline{D}_V} \quad (3)$$

3. Results and Discussion

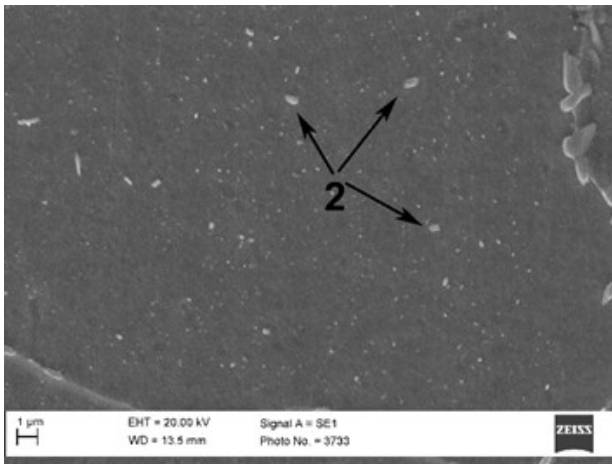
In the in-service aged material condition (ISA), the microstructure (figure 3(a)) is composed of ferrite-pearlite, in which the lamellar nature of the pearlite and the precipita-

tion inside the ferrite and in the grain boundaries are distinguished. This type of microstructure is common in low alloy Cr-Mo steels, yet Yang et al. [22] has observed this microstructure in 2.25Cr1Mo steel of steam pipelines exposed to long-term service. However, Afrouz et al. [23] reported the same microstructure in specimens from new steam pipelines subjected to creep test. In the in-service-aged material condition affected only by a simulated PWHT (condition ISA+PWHT), a microstructure (Figure 3(b)) qualitatively similar to the one from the ISA condition is observed, although some precipitates inside the ferrite are larger compared to those observed in the ISA condition.

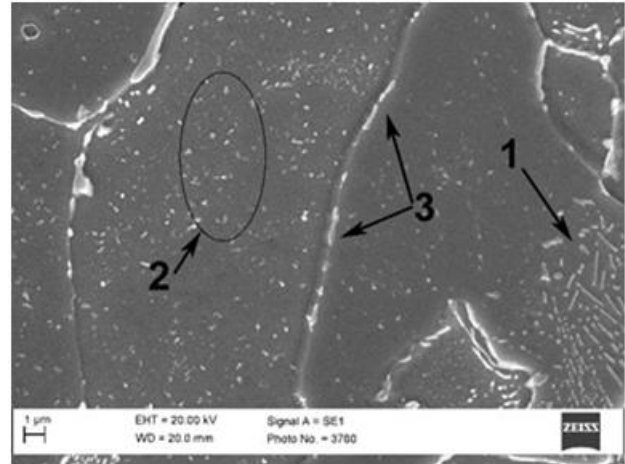
WHT conditions is also observed, regardless the undergone aging treatment (table 2). According to these results, it can be inferred that neither the PWHT nor the thermal aging qualitatively modifies the type of microstructure of the material previously in-service (aged material): ferrite-pearlite with precipitation within ferrite grains and in the grain boundary, accompanied by lamellar pearlite



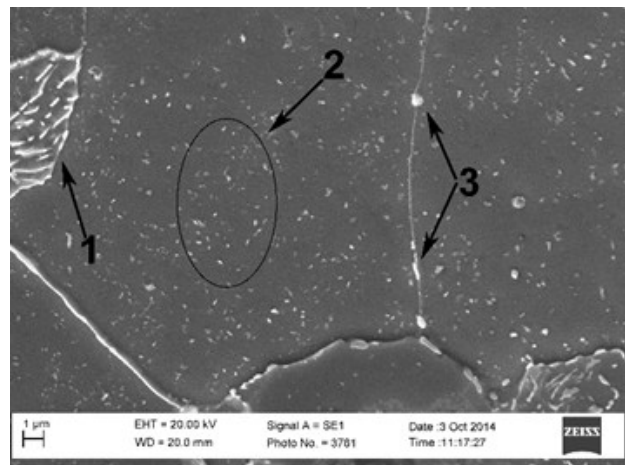
(a)



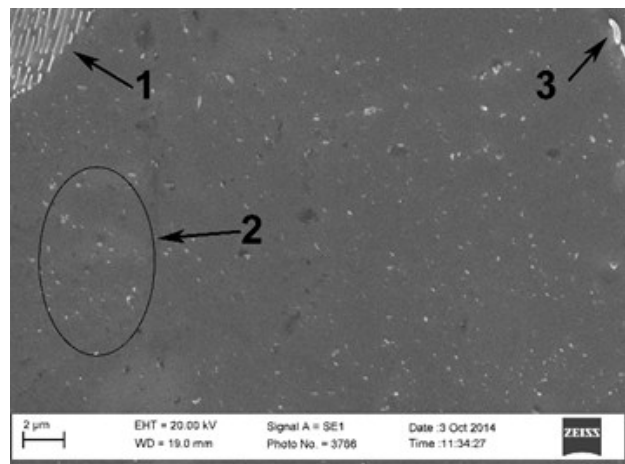
(b)



(a)



(b)



(c)

Figure 3. Representative SEM images of the material in the conditions

Note: (a) ISA; (b) ISA+PWHT, where: 1- lamellar pearlite; 2- with-in-ferrite-grain precipitates; and 3- grain boundary precipitates.

Taking now the samples from the third condition, i.e., in-service-aged material subjected to a heat treatment simulating a PWHT and also exposed to artificial aging conditions (ISA+PWHT+AA - n), a microstructure (Figure 4) qualitatively similar to those of the ISA and ISA+P-

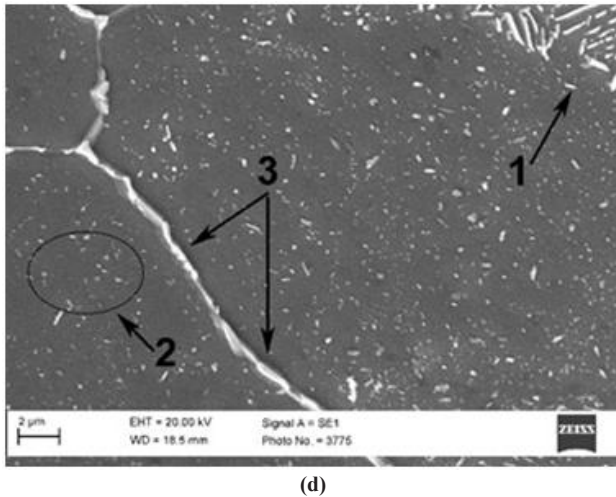


Figure 4. Representative SEM images of the material in the conditions (according to table 2)

Note: (a) ISA+PWHT+AA -1; (b) ISA+PWHT+AA -2; (c) ISA+PWHT+AA -3; and (d) ISA+PWHT+AA -4, where 1- lamellar pearlite, 2 – within-ferrite-grain precipitates and 3 – grain boundary precipitates.

The fact that the microstructures have not been modified qualitatively due to the effect of thermal aging does not mean that quantitative changes have not occurred, which are sometimes difficult to appreciate in SEM images. Among these changes, the variation of the type, size, quantity and volume fraction of precipitates within ferrite grains stands out. Regardless of whether there has been any change in the type of precipitates within ferrite grains or not, it is essential to know the other potential changes associated with them, since they intervene in the behavior of the mechanical resistance of the ferritic matrix (due to its precipitation hardening effect^[24]), and because ferrite is the majority constituent of the alloy.

Figure 5 presents the relative frequency histograms and the particle probability density curves of the in-service-aged material condition (ISA) and the in-service-aged material after PWHT (ISA+PWHT). The particle probability density curves were raised by fitting curves to the experimental data, in which an adequate fitting to a lognormal probability density function is observed in both cases (c.o.d = 0.998 and $p < 0.001$ for the ISA condition and c.o.d = 0.999 and $p < 0.001$ for the ISA+PWHT condition).

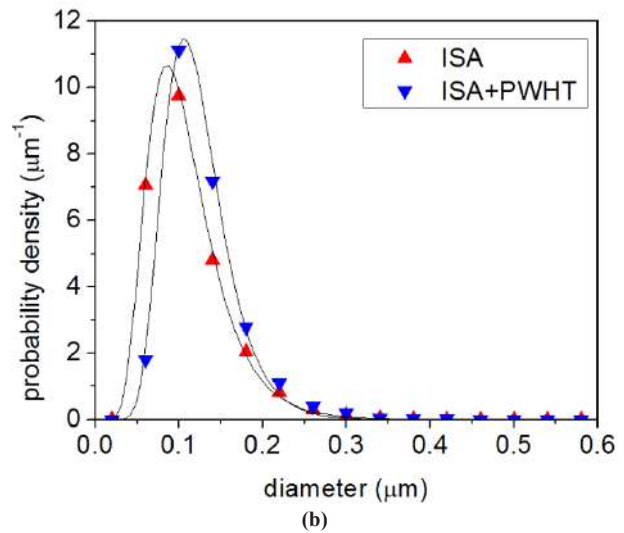
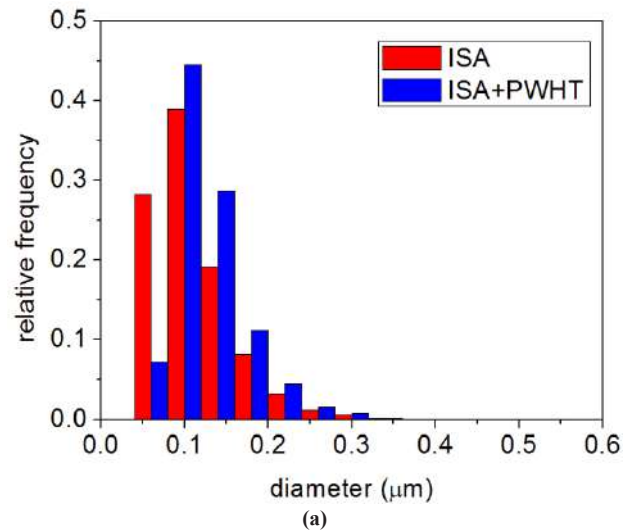


Figure 5. ISA and ISA+PWHT conditions: (a) - Relative frequency histograms of 2D size of within-ferrite-grain precipitates; (b) - particle probability density curves of the conditions

Based on the comparison of the histogram trends (figure 5 a), a quantitative effect of in-service PWHT on the 2D size distribution of within-ferrite-grain precipitates was evidenced. As seen, the relative frequency of the smaller class (0.04–0.08 μm) decreases considerably, while it increases at the remaining classes. In relation to the probability density function (figure 5 b), it is evident that the PWHT modifies the fitted curve, resulting in an increase of the mode (from 0.088 μm for the ISA condition to 0.105 μm for the ISA+PWHT condition), as well as the geometric mean diameter (from 0.101 μm for the ISA condition to 0.117 μm for the ISA+PWHT condition).

Figures 6 and 7, in turn, present similar charts of Figure 5 to compare the effect of ISA+PWHT and ISA+P-

WHT+AA conditions, the latter with different aging treatments, on the precipitate stereology. There were also adequate fittings to the lognormal type model for the different aging treatments (c.o.d equal to 0.994, 0.999, 0.992 and 0.998, respectively for the conditions ISA+PWHT+AA -1, ISA+PWHT+AA -2, ISA+PWHT+AA -3 and ISA+PWHT+AA -4, with $p < 0.001$ for all the cases). These results indicate that the thermal aging does not change the behavior observed in the ISA+PWHT condition, showing no significant variation of the relative frequency histogram of 2D size and the same particle probability density curves, keeping the value of the mode and the geometric mean diameter approximately equal under all conditions (0.1049 and 0.1170 μm , respectively).

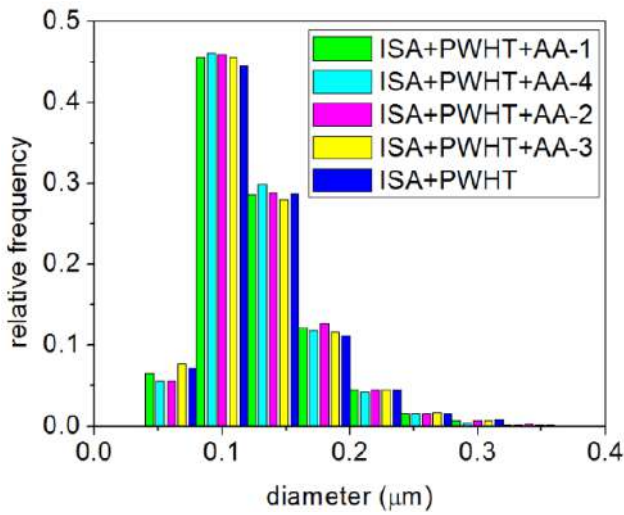


Figure 6. Relative frequency histograms of 2D size of within-ferrite-grain precipitates for the ISA+PWHT and ISA+PWHT+AA conditions, the latter as different aging treatments (according to table 2)

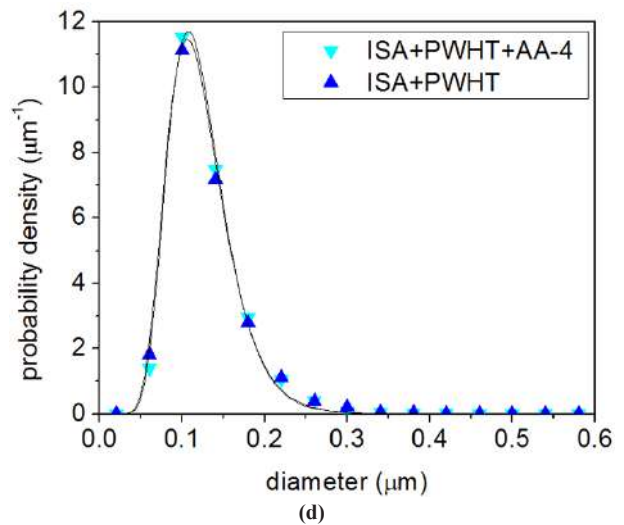
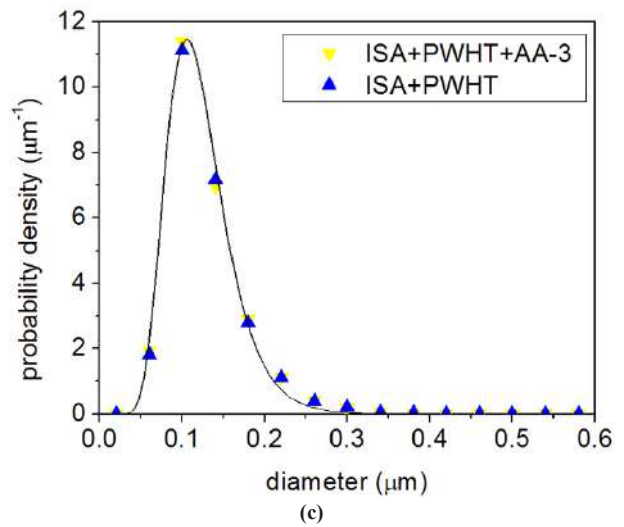
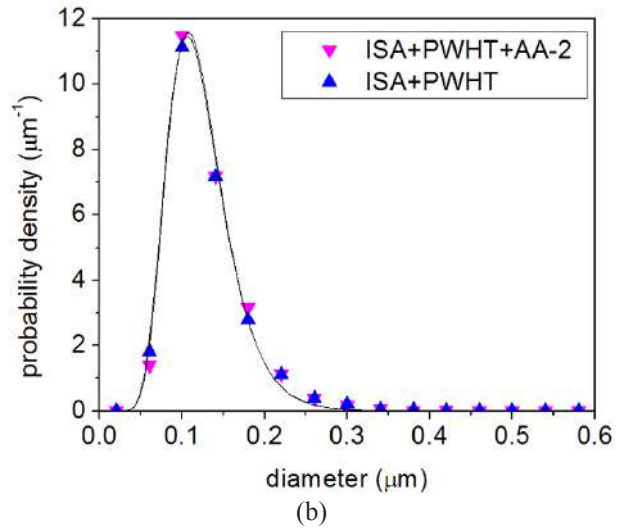
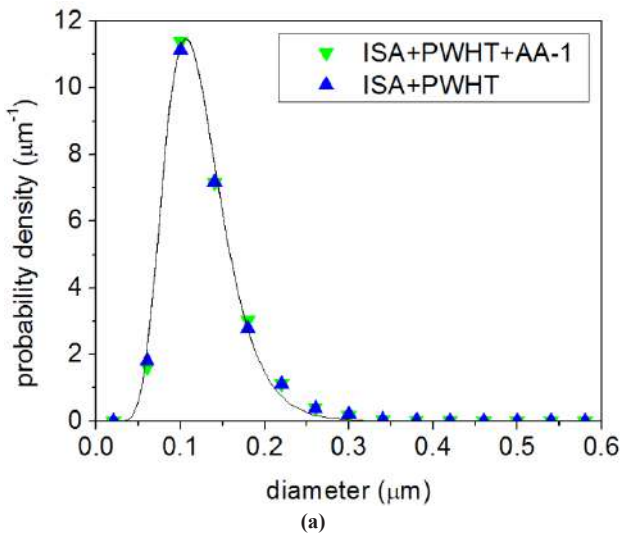


Figure 7. Particle probability density curves of the ISA+PWHT and ISA+PWHT+AA conditions, the latter at different aging treatments (according to table 2)

According to current literature [18,25], variations on the size distribution of precipitates can be associated with:

(1) precipitation of more stable particles: metastable precipitates that dissolve while nucleation and growth of more stable precipitates occurs (the amount of precipitates per unit volume is conserved and the average size and volume fraction are increased) or,

(2) coarsening processes: the growth of large precipitates at the expense of smaller ones which disappear (the volume fraction is conserved, the quantity of particles per unit volume decreases and the average size increases).

Therefore, and based on the stereological evaluation presented in Table 2, it can be stated that the coarsening process has been revealed in the present analysis, since there was an increase in the average size of the precipitates and decrease in their quantities per unit volume when the heat treatment to simulate the PWHT was applied on the long-term operation sample, yet keeping the values of the volume fraction similar. According to the results of Table 2, it can also be inferred that the PWHT stabilizes the precipitates within the ferrite grains, since the subsequent thermal aging treatments do not impose significative changes in the precipitates average sizes, in the quantities per unit of volume and the volume fractions.

Table 2. Within-ferrite-grain precipitate stereological parameters for the different material conditions

Condition	Stereological parameters		
	Mean Size 3D D_v (μm)	Quantity per unit of volume N_v (μm^{-3})	Volume fraction V_v (%)
ISA	0.147 \pm 0.015	70 \pm 8	3.1 \pm 0.5
ISA+PWHT	0.185 \pm 0.022	30 \pm 5	2.8 \pm 0.4
ISA+PWHT+AA -1	0.182 \pm 0.0183	33 \pm 3	2.6 \pm 0.4
ISA+PWHT+AA -2	0.186 \pm 0.022	31 \pm 4	2.3 \pm 0.5
ISA+PWHT+AA -3	0.183 \pm 0.020	28 \pm 4	3.0 \pm 0.5
ISA+PWHT+AA -4	0.188 \pm 0.023	31 \pm 3	2.2 \pm 0.4

5. Conclusions

The results of this work showed that the simulated PWHT applied over a sample of a 1.25Cr0.5Mo steel steam pipeline after service-aged for more than 20 years at 480 °C led to a coarsening process. Consequently, the precipitates within ferrite grains increased in size, from 0.147 \pm 0.015 to 0.185 \pm 0.022, counterbalanced by a decrease in the number of precipitates per volume unit (from 70 \pm 8 to 30 \pm 5), keeping the volumetric fraction. In addition, simulated post aging heat treatments of the samples which underwent a simulated PWHT showed to stabilize the within-ferrite-grain precipitates, with no further changes

of their stereological parameters.

Acknowledgments

This work was supported by the bilateral agreement CAPES - Brazil / MES – Cuba (project number 146/12) and carried out at the Brazilian research laboratories LA-PROSOLDA-LDTAD from Federal University of Uberlandia (UFU) and DEMa-CCDM from Federal University of Sao Carlos (UFSCar).

References

- [1] E. Keim, D. Lidbury, Review of assessment methods used in nuclear plant life management, NULIFE Report. 2012, 12 (5): 70-81.
- [2] G. Rigueira, H. Furtado, M. Lisboa, L. Almeida, Microstructural evolution and hardness changes in bainite and pearlite in Cr1Mo 2.25 steels after aging treatment. Revista Matéria, 2011, 16 (4): 857-867. DOI: 10.1590/S1517-70762011000400007
- [3] F. Abe, Precipitate design for creep strengthening of 9% Cr tempered martensitic steel for ultra-supercritical power plants, Science and Technology of Advanced Materials, 2008, 9 (1): 1-15. DOI: 10.1088/1468-6996/9/1/013002
- [4] F. Larson, J. Miller, A time-temperature relationship for rupture and creep stresses. Transactions of the ASME, 1952, 74: 765-775.
- [5] H. Furtado, F. Santos, B. Cardoso, F. Matt, L. Henrique, Power plant remaining life evaluation. Key Engineering Materials, 2014, 588 (10-11): 232-242.
- [6] K. Laha, S. Chandravathi, P. Parameswaran, S. Bhanu, S. Rao, L. Mannan, Type IV cracking in modified 9Cr-1Mo steel weld joint. Metallurgical and Materials Transactions A, 2007, 38 (1): 58-68. DOI: 10.1080/09603409.2015.1137158
- [7] A. Fernández, N. Alcántara, S. Haro, I. López, Effect of in service weld repair on the performance of CrMo steel steam pipelines. Materials Research, 2006, 9 (2): 153-158. DOI: 10.1590/S1516-14392006000200008
- [8] G. Eggeler, Microstructural parameters for creep damage quantification. Acta Metallurgica et Materialia, 1991, 39 (2): 221-231. DOI: 10.1016/0956-7151(91)90270-B
- [9] Y. Kadoya, E. Dyson, M. McLean, Microstructural stability during creep of Mo- or W-bearing 12Cr steels. Metallurgical and Materials Transactions A. 2002, 33 (8): 2549-2557. DOI: 10.1007/s11661-002-0375-z
- [10] C. Lima, L. Pinto, L. de Almeida, Microstructural evolution of Cr-Mo ferritic steel (2,25Cr-1Mo) on

- long term high temperature operation - precipitates fraction calculation. In: 5th Brazilian MRS Meeting. Florianópolis, Brazil, 2006.
- [11] X. Yu, S. Babu, H. Terasaki, Y. Komizo, Y. Yamamoto, M. Santella, Correlation of precipitate stability to increased creep resistance of Cr–Mo steel welds. *Acta Materialia*, 2013, 61 (6): 2194-2206.
DOI: 10.1016/j.actamat.2012.12.040
- [12] H. Furtado, I. Le May, High temperature degradation in power plants and refineries. *Materials Research*, 2004, 7 (1): 103-110.
DOI: 10.1590/S1516-14392004000100015
- [13] C. Lima, L.Pinto, H. Furtado, L. de Almeida, M. de Souza, I. Le May, Quantitative observations of precipitation in 2.25Cr–1Mo steel exposed to different creep conditions in a power station. *Engineering Failure Analysis*, 2009, 16 (5): 1493-1500.
DOI: 10.1016/j.engfailanal.2008.09.009
- [14] American Society for Testing and Materials. ASTM A335: Standard Specification for Seamless Ferritic Alloy-Steel Pipe for High-Temperature Service. ASTM International, West Conshohocken, PA, 2011.
- [15] American Society of Mechanical Engineers. ASME Boiler and Pressure Vessel Code. Section VIII. Division 1. Rules for Construction of Pressure Vessels. ASME, 2010.
- [16] American Society for Testing And Materials. ASTM E3-11: Standard Guide for Preparation of Metallographic Specimens, ASTM International, West Conshohocken, PA, 2011.
- [17] American Society for Testing And Materials. ASTM E407-11: Standard Practice for Microetching Metals and Alloys, ASTM International, West Conshohocken, PA, 2011.
- [18] P. Di Nunzio, H. Hougard, Y. Lan, Modelling of particle growth and application to the carbide evolution in special steels for high temperature service. In: EUR 18633 — Properties and in-service performance. Luxembourg. 1999: 195.
ISBN: 9789282850442
- [19] Y. Endo, Estimate of confidence intervals for geometric mean diameter and geometric standard deviation of lognormal size distribution. *Powder Technology*, 2009, 193 (2): 154-161.
DOI: doi.org/10.1016/j.powtec.2008.12.019
- [20] R. Sultan, S. Ahmad, Comparison of parameters of lognormal distribution based on the classical and posterior estimates. *Journal of Modern Applied Statistical Methods*, 2013, 12(2): 304-313.
DOI: 10.22237/jmasm/1383279420
- [21] K. Krishnamoorthy, T. Mathew, Inferences on the means of lognormal distributions using generalized p-values and generalized confidence intervals. *Journal of Statistical Planning and Inference*, 2003, 115 (1): 103-121 .
DOI: 10.1016/S0378-3758(02)00153-2
- [22] J. Yang, Y. Huang, C. Yang, L. Horng, Microstructural examination of 2.25Cr1Mo steel pipes after extended service. *Materials characterization*, 1993, 30 (2): 75-88
DOI: 10.1016/1044-5803(93)90011-j
- [23] A. Afrouz, J. Collins, R. Pilkington, Microstructural examination of 1Cr0,5Mo steel during creep. *Metals Technology*, 1983, 10(1): 461-463,
DOI: 10.1179/030716983803291569
- [24] D. Baird, Strengthening mechanisms in ferritic creep resistant steels. In: *Creep Strength in Steel and High Temperature Alloys. Proceedings... The Iron and Steel Institute*, 1972: 207-216.
- [25] D. Ouden Mathematical Modelling of Nucleating and Growing Precipitates: Distributions and Interfaces. Dissertation at Delft University of Technology. Netherlands, 2015.



REVIEW

Synthesis, Characterization and Applications of $\text{MoO}_3\text{-Fe}_3\text{O}_4$ Nanocomposite Material

Madhukar Navgire Akash Nagare Ganesh Kale Sandesh Bhitre*

Jijamata College of Science and Arts, Bhende, Ahmednagar, Maharashtra, India

ARTICLE INFO

Article history

Received: 17 August 2019

Accepted: 21 October 2019

Published Online: 31 October 2019

Keywords:

β -cyclodextrin

Magnetic nanocomposite

Heterogeneous catalyst

Acid-Catalyzed

Organic reactions

ABSTRACT

In the present investigation, a series of nanocomposite material such as MoO_3 , Fe_3O_4 synthesized by co-precipitation method and Beta cyclodextrin (β -CD) doped $\text{MoO}_3\text{-Fe}_3\text{O}_4$ and Graphite doped $\text{MoO}_3\text{-Fe}_3\text{O}_4$ have been synthesized successfully by Sol-Gel method. Synthesized nanomaterials were characterized in detail by XRD, FT-IR, TEM-HRTEM, UV-Vis DRS techniques. The crystalline size was in the range of 10 ± 2 nm. The activity of the prepared material as a heterogeneous catalyst was successfully tested on the organic reaction of synthesis of substituted m-Chloro-Nitrobenzene and it was found to give excellent yield.

1. Introduction

Ferromagnetic nanoparticles have gained considerable importance due to their large surface area, high reactivity, stability and reusability^[1]. The magnetic ionic liquids and magnetizable complex have been used as catalysts in oxidative reaction to enhance separation efficiency^[2-6]. Various Fe_3O_4 based catalyst have been reported by surface modification of zeolites, carbon nanotubes, activated carbon, cyclodextrin etc.^[7-10].

Research has been carried out for the development of supported and un-supported molybdenum, ceria and magnetite nanoparticles^[11-15]. In general, both molybdenum and iron based oxide catalysts have been widely used in many important oxide or acid catalytic reactions

as they are useful in several industrial processes involving organic reactions^[16-20].

The conventional liquid acids and Lewis acids have significant environmental risks. Hence, there is a growing demand for developing eco-friendly strong solid acid catalysts. The inorganic solid acid-catalyzed organic transformations are widely studied because of easy product isolation, high selectivity, easy recovery and recyclability of the catalysts and minimum waste^[21,22]. It has also been observed that metal oxide and mixed metal oxide play an important role in catalytic processes to speed up chemical reactions in an eco-friendly and cost effective manner^[23].

In view of the above facts, this paper deals with the synthesis of MoO_3 and Fe_3O_4 , nanocomposite catalytic

*Corresponding Author:

Sandesh Bhitre,

Jijamata College of Science and Arts, Bhende, Ahmednagar, Maharashtra, India;

Email: sandesh.bhitre@rediffmail.com

material by co-precipitation method and Beta cyclodextrin (β -CD) doped $\text{MoO}_3\text{-Fe}_3\text{O}_4$ and Graphite doped $\text{MoO}_3\text{-Fe}_3\text{O}_4$ nanocomposite catalytic material by Sol-gel method. This is followed with analysis of characterization carried out by XRD, FT-IR, TEM-HRTEM, UV-Vis DRS techniques of the synthesized nanocomposite catalytic material. The synthesized nanocomposite catalyst exhibited high catalytic efficiency for the organic synthesis of substituted m-Chloro-Nitrobenzene and could be quickly separated and recovered by an external magnetic field.

2. Synthesis of Catalyst

The analytical reagents (AR) used for the synthesis were, Ferrous Sulphate (Ranbaxy Fine chemicals), Ferric Sulphate (Ranbaxy Fine chemicals), Ammonium heptamolybdate (Ranbaxy Fine chemicals), Ammonia (SD Fine chemicals), Polyethylene Glycol (SD Fine chemicals), β -Cyclodextrin (β -CD) (Qualigens) and Cetyl Trimethyl Ammonium Bromide (Qualigens) without further purification.

2.1 Synthesis of MoO_3

MoO_3 was synthesized by co-precipitation technique. Ammonium heptamolybdate (2.47 gm) was dissolved in doubled distilled water and then CTAB (1.4 gm) was added to this solution. Then aqueous ammonia (1:1) was added with constant stirring. Excess water was removed by heating the precipitate for 4 hours and dried at 110°C for 2 hours. The material was crushed and calcined at 500°C for 2 hours^[24].

2.2 Synthesis of Fe_3O_4

Fe_3O_4 was synthesized by co-precipitation technique. Fe_3O_4 solution was obtained by dissolving Ferrous Sulphate (2.78gm) and Ferric Sulphate (3.99gm) in distilled water separately and mixed together under vigorously stirring until clear solution was obtained. Then 0.4gm PEG and 1.4 gm. CTAB added into this solution mixed and heated in water bath. Then precipitate was obtained by adding aqueous ammonia solution drop wise (about 10 ml). Excess water was removed by heating the precipitate for 4 hours and dried at 110°C for 2 hours. The material was crushed and calcined at 500°C for 2 hours

2.3 Synthesis of $\text{MoO}_3\text{-Fe}_3\text{O}_4$

$\text{MoO}_3\text{-Fe}_3\text{O}_4$ was synthesized by Sol-gel technique. A solution containing ammonium heptamolybdate (2.47 gm), Ferrous sulphate, (2.78 gm) and Ferric Sulphate (3.99 gm) was mixed with 150 ml distilled water. Cetyl

Trimethyl Ammonium Bromide (2.8 gm) was then added to this solution, mixed and heated in water bath. Then precipitate was obtained by adding aqueous ammonia solution drop wise (about 10 ml). Excess water was removed by heating the precipitate for 4 hours and dried at 110°C for 2 hours. The material was crushed and calcined at 500°C for 2 hours

2.4 Synthesis Of β -CD doped $\text{MoO}_3\text{-Fe}_3\text{O}_4$

β -CD doped $\text{MoO}_3\text{-Fe}_3\text{O}_4$ was synthesized by Sol-gel method. Ferrous sulphate (2.78 gm) and ferric sulphate (3.99 gm) were dissolved in deionized water separately and then mixed together with vigorously stirring. The stirring was continued until a clear solution was obtained. Then 2.470 gm of ammonium heptamolybdate, 1 gm of β -CD, 2.8 gm of CTAB and 1 gm of PVA was added to it. The above solution was then heated in water bath with constant stirring and adding iso-butanol. The pH was maintain at 8 by adding aqueous ammonia drop wise while heating and stirring the mixture for 4 hours at about 1980-2000 RPM. The obtained solution was then dried at 110°C for 2 hour. The material was crushed and calcined at 500°C for 2 hours.

2.5 Synthesis of Graphite doped $\text{MoO}_3\text{-Fe}_3\text{O}_4$

Graphite doped $\text{MoO}_3\text{-Fe}_3\text{O}_4$ was synthesized by Sol-gel method. Deionized water (150 ml) and iso-butanol (10 ml) was mixed thoroughly with ferrous sulphate (2.78 gm), ferric sulphate (3.99 gm), ammonium heptamolybdate (2.47 gm), poly vinyl alcohol (1 gm), CTAB (2.8 gm) and graphite (1 gm). Then it was then constantly stirred at 90°C and ammonia was added drop wise to maintain the pH-8. Excess water was removed by heating the precipitate for 4 hours and dried at 110°C for 2 hours. The material was crushed and calcined at 500°C for 2 hours.

3. Characterizations

3.1 XRD- Analysis

The X-ray diffraction analysis (XRD) of the prepared samples were obtained with a Philips X-ray diffractometer in the diffraction angle range $2\theta^\circ = 20$ to 80 using $\text{CuK}\alpha$ radiation of wavelength 1.5405 \AA .

Figure 1(a) shows the XRD pattern of Fe_3O_4 indicating its crystal structure, phase and lattice modification. The peaks are positioned at $2\theta^\circ = 30.08, 33.73, 37.07, 44.46, 47.15, 50.99, 54.62, 59.23, 63.62$ and 70.95 indicating hkl values due to planes (220), (310), (311), (322), (400), (332), (430), (432), (441) and (620). These peaks

were indexed as cubic Fe_3O_4 as per JCPDS database card number 79-1715 with lattice parameter $a=b=c$ 8.394 Å. Crystallite size calculated by using Debye-Scherrer equation was found to be 8.80 nm^[26].

Figure 1(b) is the XRD pattern obtained of MoO_3 that shows peaks at $2\theta^\circ = 23.33, 25.70, 33.12, 38.83, 42.39, 49.99, 52.83, 62.90, 64.92, 72.87$ and 79.87 corresponding to the planes (110), (040), (101), (060), (141), (230), (080), (251), (190), (232) and (1 11 0) indicating orthorhombic crystal structure. All the peaks are of MoO_3 as matched from the JCPDS card 76-1003^[25] and suggest that the prepared material possess crystalline in nature. The lattice parameters are $a=3.96, b=13.85$ and $c=3.69$ Å and crystallite size was found to be 42.21 nm.

The Figure 1(c) is XRD pattern for β -CD doped $\text{MoO}_3\text{-Fe}_3\text{O}_4$ nanocomposites. The diffraction peaks were observed at $2\theta^\circ = 25.88, 32.72, 42.38, 36.13, 48.95, 54.51, 63.48, 65.49, 72.82$ indexed to hkl planes (122), (400), (503), (035), (414), (718), (441), (531), (443) which indicate the monoclinic symmetry. All the reflection peaks could be indexed to monoclinic symmetry with lattice constants of $a=15.72$ Å, $b=9.24$ Å, and $c=18.22$ Å matched with JCPDS file Card No. 35-0183 are in good agreement with the literature values^[27]. The sharp and distinct peaks suggest that synthesized nanocomposite were highly crystalline, with no impurity peak and are unaffected due to coating with β -CD. The crystallite size was found to be 7.62 nm.

The Figure 1(d) shows that X-Ray diffraction results for graphite doped $\text{MoO}_3\text{-Fe}_3\text{O}_4$ nanocomposites^[28]. All peaks matched the peaks of β -CD doped $\text{MoO}_3\text{-Fe}_3\text{O}_4$ nanocomposites and the diffraction peaks were indexed with JCPDS card 35-0183 and crystallite size was found to be 6.35 nm.

Crystallite size of all samples was calculated by using Debye-Scherrer equation. The crystallite size mentioned is the average of crystallite size calculated using FWHM of three highest intensity peaks.

Table 1. Crystallite size of all samples

Sr. No.	Catalyst	Crystallite Size in nm
1	Fe_3O_4	8.80
2	MoO_3	42.21
3	β -CD doped $\text{MoO}_3\text{-Fe}_3\text{O}_4$	7.62
4	Graphite doped $\text{MoO}_3\text{-Fe}_3\text{O}_4$	6.35

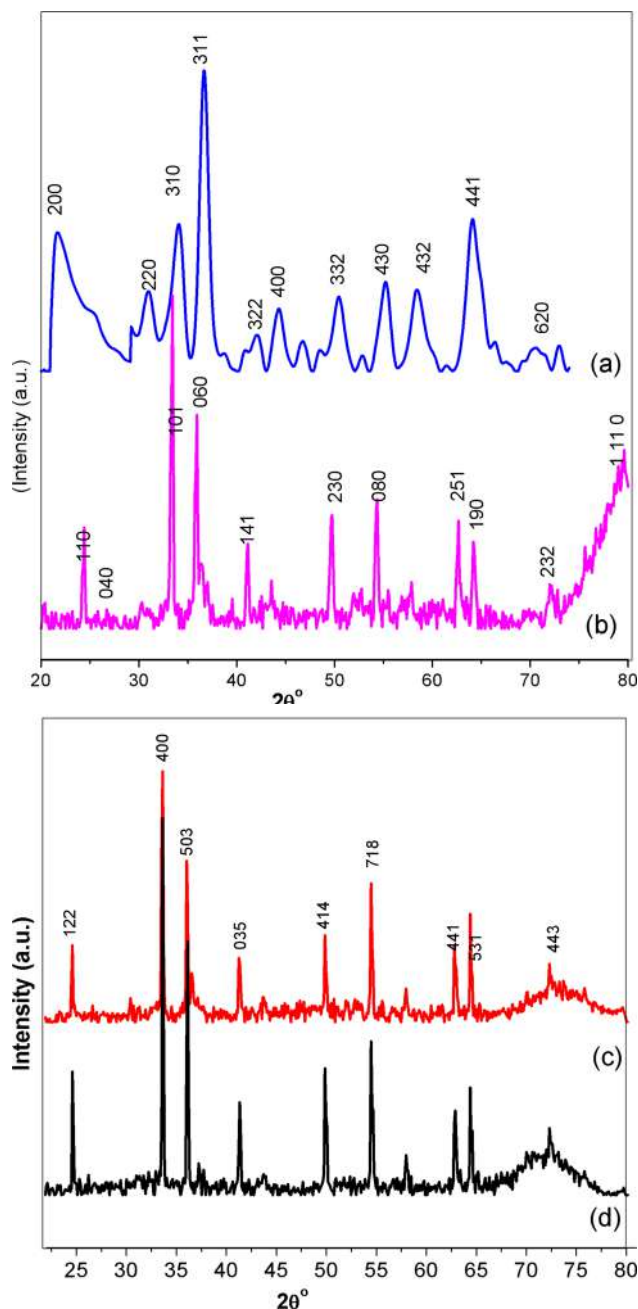


Figure 1. XRD of (a) Fe_3O_4 , (b) MoO_3 , (c) β -CD doped $\text{MoO}_3\text{-Fe}_3\text{O}_4$, (d) Graphite doped $\text{MoO}_3\text{-Fe}_3\text{O}_4$

3.2 FT-IR Analysis

The FT-IR was recorded on FT-IR spectrometer (Perkins Elmer) in the range $4000\text{-}400\text{ cm}^{-1}$. The Figure 2(a) of Fe_3O_4 shows sharp band that appears at 803 cm^{-1} is due to Fe=O bond. The band at 1143 cm^{-1} shows the M-O-M stretching. The Figure 2(b) of MoO_3 shows strong vibrations at 516 cm^{-1} due to the stretching mode of Mo-Mo bonding. Coordinated crystalline water is most likely present as seen from the H-O-H bonding vi-

bration at 1145 cm^{-1} [29].

The Figures 2(c-e) shows the FT-IR spectrum of $\text{MoO}_3\text{-Fe}_3\text{O}_4$, $\beta\text{-CD}$ doped $\text{MoO}_3\text{-Fe}_3\text{O}_4$ and graphite doped $\text{MoO}_3\text{-Fe}_3\text{O}_4$ respectively. The peaks measured for all samples are over the range of $4000\text{-}500\text{ cm}^{-1}$. The peaks at $771, 787, 803\text{ cm}^{-1}$ are because of stretching and bending mode of oxygen in Fe-O-Fe, Mo-O-Mo, Mo=O and Fe=O bonds which indicates the specification of a layered orthorhombic MoO_3 phase and the presence of FeO and Fe_2O_3 . Strong vibrations were detected at $516, 531$ and 539 cm^{-1} which corresponds to formation of bond between $\text{MoO}_3\text{-Fe}_3\text{O}_4$. The band around $1128, 1145, 1120\text{ cm}^{-1}$ is due to co-ordinated crystalline water most likely present due to H-O-H bending vibrations.

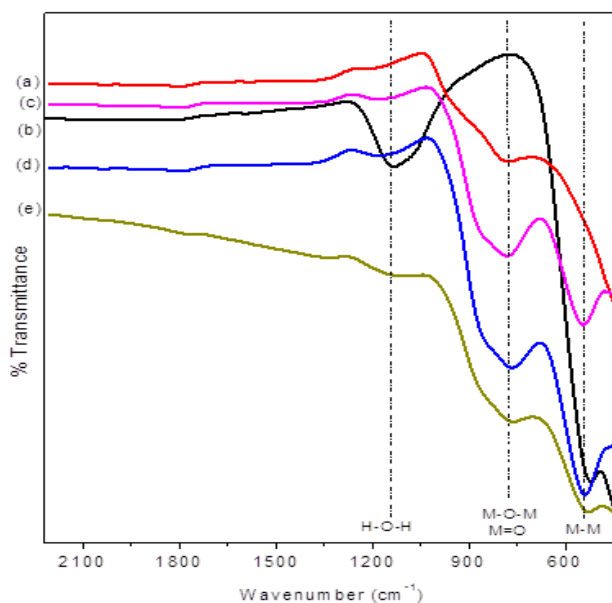


Figure 2. FT-IR spectrums of (a) Fe_3O_4 , (b) MoO_3 , (c) $\text{MoO}_3\text{-Fe}_3\text{O}_4$, (d) $\beta\text{-CD}$ doped $\text{MoO}_3\text{-Fe}_3\text{O}_4$, and (e) graphite doped $\text{MoO}_3\text{-Fe}_3\text{O}_4$

3.3 TEM-HRTEM Analysis

The TEM and HRTEM images were obtained for $\beta\text{-CD}$ doped $\text{MoO}_3\text{-Fe}_3\text{O}_4$, and Graphite doped $\text{MoO}_3\text{-Fe}_3\text{O}_4$. Figure 3(a) for $\beta\text{-CD}$ doped $\text{MoO}_3\text{-Fe}_3\text{O}_4$ exhibits uniform size distribution and high crystalline nature with size range of $10 \pm 2\text{ nm}$, matching with the XRD data which is 8.96 nm . The diffraction spots and rings in SEAD pattern show that the distance from the center of the rings to the diffraction spots are 0.29 nm for (101) planes of MoO_3 and 0.25 nm for (311) planes of Fe_3O_4 .

Figure 3(b) for graphite doped $\text{MoO}_3\text{-Fe}_3\text{O}_4$ also exhibits uniform size distribution and high crystalline

nature with size range of $10 \pm 2\text{ nm}$, matching with the XRD data which is 9.83 nm . The SEAD pattern shows diffraction spots and rings at (101) planes of MoO_3 and (311) planes of Fe_3O_4 .

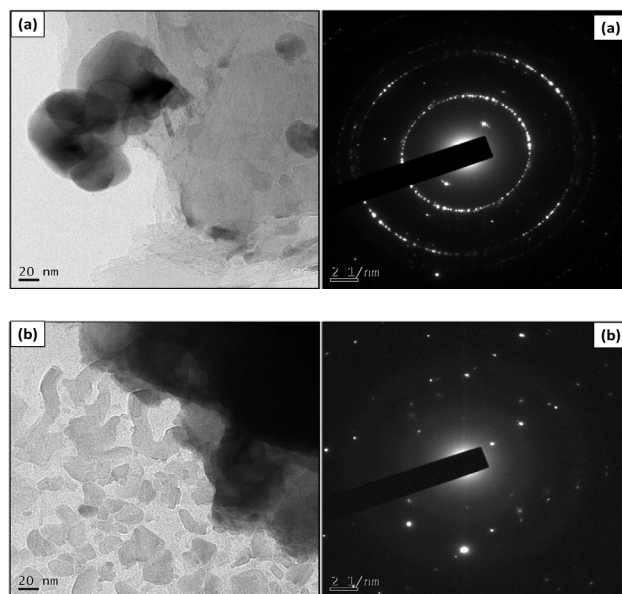


Figure 3. TEM-HRTEM images of (a) $\beta\text{-CD}$ doped $\text{MoO}_3\text{-Fe}_3\text{O}_4$, and (b) Graphite doped $\text{MoO}_3\text{-Fe}_3\text{O}_4$

3.4 UV-Visible DRS Analysis

UV-Visible DRS Analysis was done using Varian Cary (5000) spectrometer in the range of $800\text{-}200\text{ nm}$ and the same are shown in Figure 4. The spectrums show maximum reflectance between $300\text{-}450\text{ nm}$.

The MoO_3 absorbs light of wavelength 351 nm with band gap of around 3.53 eV , Fe_3O_4 absorbs light of wavelength 346 nm with band gap of around 3.58 eV , $\text{MoO}_3\text{-Fe}_3\text{O}_4$ absorbs light of wavelength 348 nm with band gap of around 3.57 eV , $\beta\text{-CD}$ doped $\text{MoO}_3\text{-Fe}_3\text{O}_4$ absorbs light of wavelength 338 nm with band gap of around 3.67 eV and Graphite doped $\text{MoO}_3\text{-Fe}_3\text{O}_4$ absorbs light of wavelength 324 nm with band gap of around 3.83 eV [30]. MoO_3 absorbs light beyond 346 nm due to lower band gap. Interestingly it was observed for modified $\beta\text{-CD}$ doped $\text{MoO}_3\text{-Fe}_3\text{O}_4$ and Graphite doped $\text{MoO}_3\text{-Fe}_3\text{O}_4$ that they absorb of light of wavelengths at 338 nm and 324 nm indicating shift from higher wavelength to lower wavelength that is blue shift. The increase in band gap from 3.53 eV for MoO_3 and 3.58 eV for Fe_3O_4 to 3.67 eV for $\beta\text{-CD}$ doped $\text{MoO}_3\text{-Fe}_3\text{O}_4$ and 3.83 eV for Graphite doped $\text{MoO}_3\text{-Fe}_3\text{O}_4$ indicates greater stability of the doped samples.

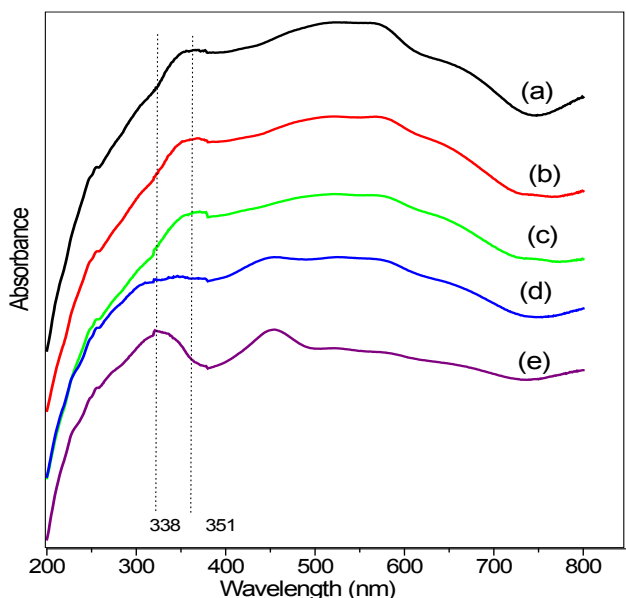
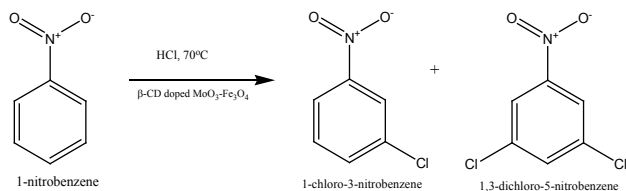


Figure 4. UV-Visible DRS spectrums of (a) MoO_3 , (b) Fe_3O_4 , (c) $\text{MoO}_3\text{-Fe}_3\text{O}_4$, (d) $\beta\text{-CD}$ doped $\text{MoO}_3\text{-Fe}_3\text{O}_4$, and (e) graphite doped $\text{MoO}_3\text{-Fe}_3\text{O}_4$

4. Catalytic Activity Results

The catalytic activity of the synthesized material was examined considering the model reaction of nucleophilic one-pot substitution reaction. The reaction of nitrobenzene (1.0 mmol) with concentrated hydrochloric acid and 0.1 g of catalyst in ethyl alcohol (10 mL) as solvent was carried out at 70°C . The Table 2 shows effect of catalyst on substitution reaction. Among the catalysts $\beta\text{-CD}$ doped $\text{MoO}_3\text{-Fe}_3\text{O}_4$ exhibited very good activity in the synthesis of substituted m-Chloro-Nitrobenzene with excellent yield in very short reaction time as compared to the others. This is attributed to the nano-crystalline size and high porosity of $\beta\text{-CD}$ doped $\text{MoO}_3\text{-Fe}_3\text{O}_4$. In this reaction 93% conversion was observed in 120 minutes which is better in comparison with earlier reported methods.

The predicted mechanism for synthesis of substituted m-Chloro-Nitrobenzene by using $\beta\text{-CD}$ doped $\text{MoO}_3\text{-Fe}_3\text{O}_4$ catalyst is presented in Scheme 1.



Scheme 1. Proposed Mechanism for the preparation of substituted m-Chloro-Nitrobenzene

Table 2. Effect of catalyst on substitution reaction

Entry	Catalyst	Time in minute	Yield/%
1	No Catalyst	No product	0
2	MoO_3	180	78
3	Fe_3O_4	180	58
4	$\text{MoO}_3\text{-Fe}_3\text{O}_4$	180	64
5	$\beta\text{-CD}$ doped $\text{MoO}_3\text{-Fe}_3\text{O}_4$	120	93, 93, 92 ^a
6	Graphite doped $\text{MoO}_3\text{-Fe}_3\text{O}_4$	180	88

Note: Reaction condition: Nitrobenzene (1.0 mmol), Conc. HCl, catalyst (0.1gm), ethyl alcohol (10 mL), temperature (70°C).

^a Product yield with catalyst reused for third time.

Physical and spectroscopic data

1-chloro-3-nitrobenzene: ^1H NMR (DMSO, 300 MHz) δ : 8.40 (s, $J = 2.0\text{Hz}$ 1H), 8.07 (ddd, $J = 8.0, 2.0$ and 2.0Hz 1H), 7.66 (ddd, $J = 8.0, 2.0$ and 2.0Hz 1H), 7.46 (dd, $J = 8.0\text{Hz}$, 1H); FT-IR (Diamond ATR) ν : 3397, 1594, 1166 and 535 cm^{-1} . $\text{C}_6\text{H}_4\text{ClNO}_2$, Exact Mass: 156.99, Mol. Wt.: 157.55, m/e : 156.99 (100.0%), 158.99 (32.0%), 158.00 (6.6%), 159.99 (2.2%), C, 45.74; H, 2.56; Cl, 22.50; N, 8.89; O, 20.31;

Melting Point = 48°C

5. Conclusion

The nanocomposites of MoO_3 and Fe_3O_4 were synthesized successfully by co-precipitation method whereas those of $\text{MoO}_3\text{-Fe}_3\text{O}_4$, $\beta\text{-CD}$ doped $\text{MoO}_3\text{-Fe}_3\text{O}_4$ and Graphite doped $\text{MoO}_3\text{-Fe}_3\text{O}_4$ were synthesized successfully by Sol-gel method. The characterization was done by sophisticated techniques like XRD, FT-IR, TEM-HRTEM, UV-Vis DRS techniques. It was found that crystalline size for all samples was about 10 ± 2 nm. Among the synthesized nanocomposite catalytic materials $\beta\text{-CD}$ doped $\text{MoO}_3\text{-Fe}_3\text{O}_4$ exhibited very good catalytic activity for the synthesis of substituted m-chloro nitrobenzene derivatives in environment friendly conditions with excellent yield in very short reaction time, which is 93% conversion was observed in 120 minutes. The catalyst could be quickly separated and recovered by an external magnetic field.

Acknowledgements

1. University Grants Commission (WRO), New Delhi, for financial support in the form of a Minor Research Project.
2. The Principal, Jijamata College of Science and Arts Bhende, for providing the all required facilities to carry out the work.

References

- [1] L.J. Xu, J.L. Wang, dx. Environ. Sci. Technol. 2012, 46: 10145–10153.
DOI: org/10.1021/es300303f

- [2] W. S. Zhu, P. W. Wu, L. Yang, Y. H. Chang, Y. H. Chao, H. M. Li, Y. Q. Jiang, W. Jiang, S. H. Xun, *Chem. Eng. J.*, 2013, 229: 250-256.
- [3] W. Jiang, W. S. Zhu, H. M. Li, J. Xiong, S. H. Xun, Z. Zhao, Q. Wang, *RSC Adv.*, 2013, 3: 2355-2361.
- [4] Y. Nie, Y. X. Dong, L. Bai, H. F. Dong, X. P. Zhang, *Fuel*, 2013, 103: 997-1002.
- [5] Y. Z. Chen, F. W. Zhang, Y. Y. Fang, X. H. Zhu, W. L. Zhen, R. Wang, J. T. Ma, *Catal. Commun.*, 2013, 38: 54-58.
- [6] F. Wang, G. J. Wang, H. J. Cui, W. T. Sun, T. B. Wang, *Mater. Res. Bull.*, 2015, 63: 181-186.
- [7] Y. Zhou, L. Sun, H. Wang, W. Liang, J. Yang, L. Wang, S. Shuan, Investigation on the uptake and release ability of β -cyclodextrin functionalized Fe₃O₄ magnetic nanoparticles by methylene blue, *Materials Chemistry and Physics*, 2016, 170: 83-89.
- [8] C. Pizarro, M. A. Rubio, M. Escudey, M. F. Albornoz, D. Munoz, J. Denardin, J. D. Fabris, Nanomagnetite-Zeolite Composites in the Removal of Arsenate from Aqueous Systems, *J. Braz. Chem. Soc.*, 2015, 26: 1887-1896.
- [9] N. Yang, S. Zhu, D. Zhang, S. Xu, Synthesis and properties of magnetic Fe₃O₄-activated carbon nanocomposite particles for dye removal, *Materials Letters*, 2008, 62: 645-647.
- [10] A.L. Cazetta, O. Pezoti, K.C. Bedin, T.L. Silva, A.P. Junior, T. Asefa, V.C. Almeida, Magnetic Activated Carbon Derived from Biomass Waste by Concurrent Synthesis: Efficient Adsorbent for Toxic Dyes, *ACS Sustainable Chem. Eng.*, 2016, 4: 1058-1068.
- [11] ME Navgire, P Gogoi, B Malleshram, A Rangaswamy, BM Reddy, β -Cyclodextrin supported MoO₃-CeO₂ nanocomposite material as an efficient heterogeneous catalyst for degradation of phenol, *RSC Advances* 2016, 6(34): 28679-28687.
- [12] A Gogoi, M Navgire, KC Sarma, P Gogoi, Fe₃O₄-CeO₂ metal oxide nanocomposite as a Fenton-like heterogeneous catalyst for degradation of catechol, *Chemical Engineering Journal*, 2017, 311: 153-162.
- [13] A Gogoi, M Navgire, KC Sarma, P Gogoi, Highly efficient heterogeneous Fenton activities of magnetic β -cyclodextrin (Fe) framework for Eriochrome black T degradation, *Materials Chemistry and Physics*, 2019, 231: 233-243.
- [14] A Gogoi, M Navgire, KC Sarma, P Gogoi, Synthesis and characterization of β -cyclodextrin coated Fe₃O₄/carbon nanocomposite for adsorption of tea catechin from aqueous solutions, *Indian Journal of Chemical Technology*, 2017, 24(5): 498-507.
- [15] A Gogoi, M Navgire, KC Sarma, P Gogoi, Novel highly stable β -cyclodextrin fullerene mixed valent Fe-metal framework for quick Fenton degradation of alizarin, *RSC Advances*, 2017, 7, 64: 40371-40382.
- [16] J. Haber, *The Role of Molybdenum in Catalysis*, Clima Molybdenum, Ann Arbor, MI, 1981.
- [17] Madhukar E. Navgire and Machhindra K. Lande, Selective Synthesis of 2-Aryl-1-arylmethyl-1H-benzimidazoles Using Carbon doped MoO₃ as an Efficient Heterogeneous Catalyst, *International Journal of Engineering Research & Technology*, 2013, 2(10): 2313-2320.
- [18] Baig, A; Ng, F.T.T. A Single-Step Solid Acid-Catalyzed Process for the Production of Biodiesel from High Free Fatty Acid Feedstocks. *Energy Fuels*, 2010, 24: 4712-4720.
- [19] de Paiva, Jr.J.B; Monteiro, W.R; Zacharias, M.A; Rodrigues, J.A.J; Cortez, G.G. Characterization and catalytic behavior of MoO₃/V₂O₅/Nb₂O₅ systems in isopropanol decomposition. *Braz. J. Chem. Eng.*, 2006, 23: 517-524.
- [20] Rathod, S.B; Lande, M.K; Arbad, B.R. Synthesis, Characterization and Catalytic Application of MoO₃/CeO₂-ZrO₂ Solid Heterogeneous Catalyst for the Synthesis of Benzimidazole Derivatives. *Bull. Korean Chem. Soc.*, 2010, 31: 2835-2840.
- [21] Clark, J.H. *Solid Acids for Green Chemistry*. *Acc. Chem. Res.* 2002, 35: 791-797.
- [22] Okuhara, T. *Water-Tolerant Solid Acid Catalysts*. *Chem. Rev.* 2002, 102: 3641-3666.
- [23] Lande, M.K; Navgire, M.E; Rathod, S.B; Katkar, S.S; Yelwande, A.A; Arbad B.R. An efficient green synthesis of quinoxaline derivatives using carbon-doped MoO₃-TiO₂ as a heterogeneous catalyst. *J. Ind. Eng. Chem.* 2012, 18: 277-282.
- [24] M Navgire, M Lande, A Gambhire, S Rathod, D Aware, S R Bhitre, Nanocomposite materials and its photocatalytic activity *Bull. Mater. Sci.*, 2011, 34(3): 535-541.
- [25] Kihlberg L, *Ark. Kemi.* 1963, 21: 557.
- [26] Taylor, *X-ray metallography*, New York: John Wiley, 1961, 678.
- [27] Qin Zhou, Shurong Fu, Min Zou, Yiming He, Ying Wu and Tinghua Wu, *RSC Adv.*, 2015,5: 69388-69393.
- [28] V. Massarotti et al, *J. Appl. Crystallogr.* 1981, 14, 64.
- [29] A.Z.M. Badruddoza, A.S.H. Tay, P.Y. Tan, K. Hidayat, M.S. Uddin, Carboxymethyl- β -cyclodextrin conjugated magnetic nanoparticles as nano-adsorbents for removal of copper ions: synthesis and adsorption studies, *J. Hazard Mater.* 2011, 185: 1177-1186.
- [30] C. Hui, C. Shen, T. Yang, L. Bao, J. Tian, H. Ding, C. Li, H.J. Gao, Large-scale Fe₃O₄ nanoparticles soluble in water synthesized by a facile method, *J. Phys. Chem. C*, 2008, 112: 11336-11339.



ARTICLE

Behaviour of Friction Stir Dissimilar Welded Blanks and The Role of Different Tool Pin Profiles

Bhanodaya Kiran Babu Nadikudi*

Mechanical Engineering Department, Sreenidhi Institute of Science and Technology, Hyderabad, India

ARTICLE INFO

Article history

Received: 24 June 2019

Accepted: 9 September 2019

Published Online: 31 October 2019

Keywords:

Aluminium alloys

Welded blanks

Friction stir welding

Tool pin profiles

Limiting dome height test

ABSTRACT

In this study, the forming behaviour of dissimilar welded blanks was studied. Welded blanks were prepared with friction stir welding process with different types of tool pin profiles. Welded blanks were developed with fixed friction stir welding process parameters by varying the tool pin profiles. The forming behaviour of welded blanks were analyzed with the limiting dome height test in biaxial stretch forming condition. The results reveal that the formability of welded joints are made with the square pin tool exhibited a better formability behaviour when compared with other profiled tools, this is due to sufficient amount heat generation and high static volume to dynamic volume ratio.

1. Introduction

The application of Tailor welded blanks (TWBs) are generally found in the aerospace and automotive industries, where the need of a high strength to weight ratio parts for the fabrication purpose with local required stiffness at some part of the components. Aluminium metal matrix composites are capable to fulfill the requirement of high strength and low weight for particular applications. Friction stir welding (FSW) is a metal joining technique and is widely used in making of aluminium alloys welded blanks. It is a basically a solid state process, the base materials are welded together in plastic deformation condition, so that the process avoids many problems that are commonly encountered with the conventional welding techniques such as porosity, cracks

etc. TWBs can be made with same or different materials. In some cases, TWBs made with weak and strong material combination to form a component and there is a need of different strengths at different places of the component with less weights. It is not that much easy to deform a high strength material as compared with less strength material. The less strength material normally gives a better response to the applied load and not the high strength material because of difference in the ductility of materials that results in uneven deformation. Many researchers have used different kinds of metal joining techniques viz. arc welding, gas welding and friction stir welding to make welded blanks^[1,2] and are formed into required shapes^[3-5]. In the past research, FSW was applied to weld similar^[6] and dissimilar^[7-9] aluminium alloys. With this process they obtained a refined ho-

*Corresponding Author:

Bhanodaya Kiran Babu Nadikudi,

Mechanical Engineering Department, Sreenidhi Institute of Science and Technology, Hyderabad, India;

Email: uday.nadikudi@gmail.com

mogenized structure in the weld zone with superior mechanical properties. This is because of stirring action of the tool pin and extrusion of plasticized material during welding^[3]. Tool pin is considered as an important parameter^[4,10] in the FSW process, because of it stirs the material around in the joining area and develops a fine grain structure. It also avoids the voids in stir zone^[5] and also dictates the flow of plasticized material during welding^[6,7]. For good quality of TWBs, it's necessary to use a proper FSW tool pin to develop the required amount of heat by sweeping huge quantity of plasticized metal^[8]. Xu et al.^[11] studied the influence of tool pin profiles and process parameters of welded joints made with AA2219 aluminium alloys through FSW. Vijay et al.^[12] achieved a better tensile properties with use of a square profiled tool pin is mainly due to flat faces of tool pin and holding dynamic volume to static volume ratio. Morteza et al.^[13] developed welded joints using H13 tool and the rupture was observed at heat affected zone in the low strength alloy side on welded blanks during limiting dome height test. Lietao et al.^[14] analyzed the formability of FSW welded blanks made with similar and different kind of alloys using threaded tool revealed that the base material size and their properties are the main influencing parameters on the formability. According to Palanivel et al.^[15] a better welded joints can be developed using FSW process with a square pin tool and revealed that the tool profile is better to develop a good refined structure through sufficient heat development during welding. In this paper, an attempt was made to study the effect of different tool pin profiles on the properties and formability through the Limiting Dome Height (LDH) test.

2. Experimental Procedure

The base aluminium alloys used for the work were AA6061 and AA2014 alloys with blank thickness of 3mm. The composition (wt%) for AA6061-T6 aluminium alloy blank is Al- 0.8Mg- 0.45Si- 0.025Cu- 0.017Ti- 0.04Cr- 0.15Mn and for AA2014 aluminium alloy blank is Al- 3.98Cu- 0.46Mg- 0.75Si- 0.026Ti- 0.017Cr. First the two base material sheets are sliced to size of 300mm x 75mm. Friction stir welding was conducted on the vertical axis milling machine with different tool pin profiles viz. Straight Cylindrical (SC), Taper Cylindrical (TC), Stepped Cylindrical (ST), Straight Square (SS), and Straight Hexagonal (SH). FSW experiments were conducted with tool rotational speed of 900 rpm, welding speed of 24 mm/min and tool tilt angle of 1°. After welding, testing specimens were extracted from welded sheets and tensile test specimens were prepared as per standards of ASTM and tests were performed on univer-

sal tensile testing machine.



Figure 1. FSW arrangement



Figure 2. Photograph of different tool pin profiles

Forming test on welded sheets were conducted through LDH test and samples were prepared as square in size (100 mm x 100 mm). LDH test was conducted on a 50 tons hydraulic press and forming was made with 36 mm diameter hemispherical punch. The data logger which is attached to press was recorded the dome height and applied load data during forming and the arrangement of hydraulic press with punch, dies and welded blank is shown in Figure 3. It can be observed that the welded blanks made with dissimilar aluminium alloys was generally less and on the other hand, a huge weld line movement was observed. This is mainly due to difference in ductility of the two alloys. AA2014 alloy was heated in the furnace at 495 °C for one hour and immediately quenched in water. And then solutionized blanks are naturally aged for five days at room temperature. The welding was carried out with the heat treated AA2014 and as received AA6061 alloys and forming test was carried. The microstructural examination of base materials and also weld zone of the joined sheets was done with scanning electron microscope after applying the Keller's reagent to reveal the microstructures.



Figure 3. Arrangement of hydraulic press with punch, dies and welded blank

3. Results and Discussions

3.1 Formability Analysis

Figure 4 shows the effect of different tool pins on the formability of welded blanks. The material flow and developed heat are controlled with stirring action of the tool geometry^[15]. The action of the tool dictate by the ratio of dynamic to the static volume of the geometry. The values for the ratio is equal to 1 for SC tool, 1.09 for TC tool, 1 for ST tools, 1.56 for SS tool and 1.21 for SH tool^[15,17,18]. Out of five pin profiles, SS tool is holding high ratio of 1.56 with tool pin pulsating action of 60 pulses/sec is enough to develop sufficient heat to make the welding zone material soft and sweeping a huge amount of plasticized material around the pin of rotating tool, which results in a better formation of weld and led to formability enhancement. ST and TC pin profile tools holding almost a same ratio and there is possibility of less flow of plasticized material and led to decrease in the formability. The SC pin profiled tool holding the ratio of 1.0 and generates less flow of plasticized material around the pin and attained a lesser formability. This is because of the absence of pulsating action of the tool pin was experienced. Although, the SH pin tool holds ratio of 1.21 and the highest number of pulsating action, this tool pin resembles almost as a cylindrical profile tool leads to less properties.

It can be noted that, a high LDH (16.8 mm) value is obtained for welded blank developed with SS pin profiled tool and confirmed the effect of SS profiled tool is more on the weld zone properties, similar kind of observations were made by some researchers^[15,19,20]. The SH and SS pin profiled tools hold flat faces on the tool pin and devel-

oped a localized pulsating stir action to plasticize the materials around during welding. At tool rotational speed of 900 rpm, the SS profiled pin produces 60 pulses/sec, due to high pulses/sec produced is sufficient heat at weld zone and leads to better properties. The SH pin profiled tool produced a low LDH (10.8 mm) formability characteristics is due to at higher rotational speed, the SH tool flat faces are resembles as almost SC tool pin profiled tool, and developed a insufficient heat during welding. The yield strength and formability of welded blanks are relates inversely with each other. Forming behaviour of an material is a function of fundamental material properties such as strain hardening exponent (n) and work hardening capacity ($1/YR$) of that material, and existing a relation with the formability^[21,22]. Higher values 'n' are required for better welded blanks formability and are correlated with LDH values and also with $1/YR$ values. $1/YR$ values are obtained from inverse of the Yield Ratio ($YR = \text{yield strength}/\text{tensile strength}$), which is good indicator for the formability behaviour^[23]. It can be observed from Figure 5, the LDH has almost a linear relation with the elongation (e), strain hardening exponent (n) and also with the work hardening capacity ($1/YR$). On otherside, higher 'n' value was obtained for welded blanks made with SS pin profiled tool, this is mainly due favourable heating condition through pulsating action of the tool pin. These relationships are showing a good agreement of formability with tensile results.

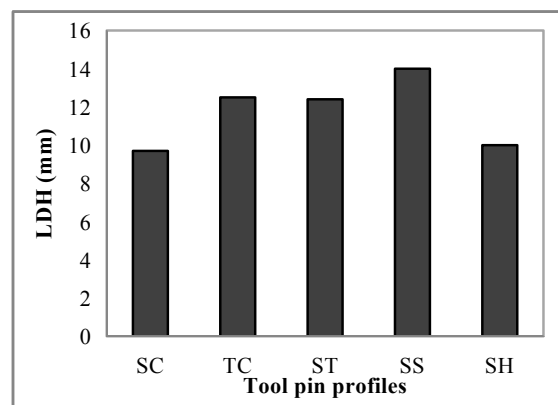


Figure 4. Effect of different tool pin profiles on the formability of the welded blanks

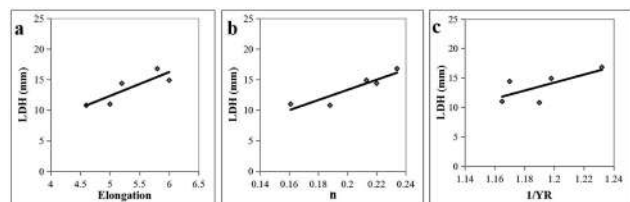


Figure 5. Variations of LDH for (a) elongation (b) strain hardening component (c) work hardening capacity of welded blanks

The recorded punch loads and dome heights during forming are plotted in Figure 6. It can be observed that the welded blank made with SS profiled tool attain high dome height with underwent more load as compared with the welded blanks made with other pin profiles.

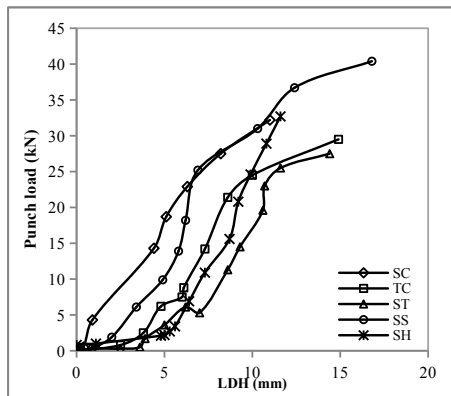


Figure 6. Punch load and limiting dome height diagram for welded blanks made with different tool pin profiles

3.2 Microstructural analysis

The microstructures of the base materials are shown in figures 7a and b respectively. Base alloy AA6061 mainly consist of particles of Al, Fe, Mn with some Mg₂Si (white) precipitates. AA2014 alloy consists of CuAl₂ precipitates (white) in aluminium matrix and also consists of some insoluble such as Fe, Mn, Si particles. The micrographs of welded zones made with different tool pin profiles are shown in Figure 8a-e. Through FSW process, homogenized and fine grains are formed at the weld zone [3,5,19], at the appropriate heat generation is result of severe plastic deformation [20,24,25]. A homogeneous and fine grained structure can observed in the case of welded blanks made with SS profiled tool. This is due to appropriate heat generation through pulsating action of the SS tool pin. A less homogenized microstructure obtained with usage of TC and ST pin tools and on otherside, coarse and unhomogenized grains were obtained with SH and SC profiled tools. This is mainly due to insufficient heat generation of the tool. This gives an effect of decreasing the formability of welded blanks.

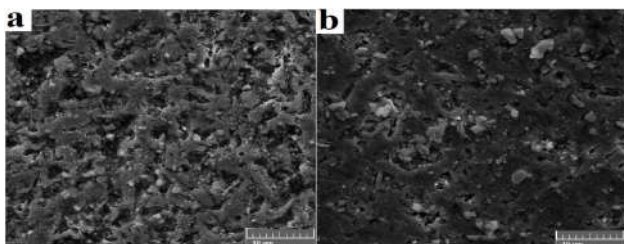


Figure 7. SEM micrographs for (a) AA6061 (b) AA2014 base materials

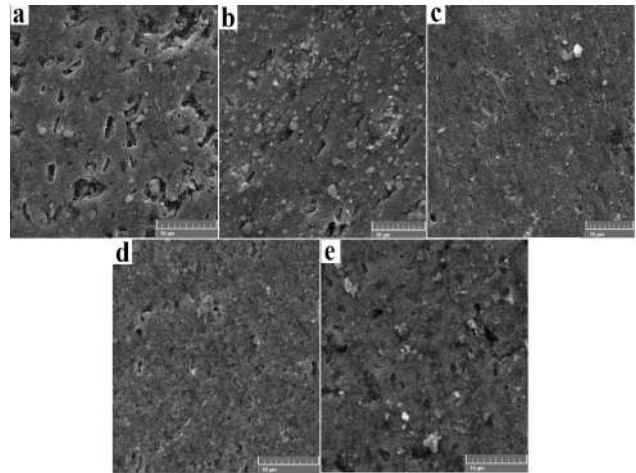


Figure 8. SEM micrographs of weld zones of (c) SC, (d) TC, (e) ST, (f) SS, (g) SH tool pin profiles

4. Conclusions

The dissimilar welded joints were developed using FSW process by using different tool pin profiles and then formability behaviour was studied with the LDH test. From the results, it can be observed that the welded joints developed using a square profile pin tool gives a better formability is due to the pulsating action of the tool produced a fine and uniform distributed grains throughout the structure and this results were confirmed from the obtained microstructure.

References

- [1] Shibata K, Iwase T, Sakamoto H, Kasukawa M, Chiba K, Saeki H. Welding of aluminium tailored blanks by Nd: YAG lasers. *Weld Int*, 2003, 17: 282-286.
- [2] Paul C. Sinclair, William R. Longhurst, Chase D. Cox, David H. Lammlein, Alvin M. Strauss, George E. Cook. Heated friction stir welding: an experimental and theoretical investigation into how preheating influences process forces. *Mater Manuf Process*, 2010, 25: 1283-1291.
- [3] Endre Romhanji, Vencislav Grabulov. Deformation behaviour of welded stainless steel – carbon steel sandwich sheet material. *Sci Tech Rev*, 2007;LVII:3-7.
- [4] Sushanta Kumar Panda, Ravi Kumar D. Study of formability of tailor-welded blanks in plane-strain stretch forming. *Int J Adv Manuf Technol*, 2009, 44: 675-685.
- [5] Joon Sik Park, Kyoung Mook Lim. Effect of laser welding variables on the formability of 3 wt% Si-added steel welds. *Mater Manuf Process*, 2009, 24: 431-437.

- [6] Subbaiah K, Geetha M, Govindaraju M, Koteswara rao SR. Mechanical properties of friction stir welded cast Al-Mg-Sc alloys. *Trans Indian Inst Met*, 2012, 65: 155-158.
- [7] Xiandong Xu, Xinqi Ynag, Gngang Zhou, BoTan. The mixing condition and mechanical property on friction stir welded dissimilar formed 3003 and 6061 aluminium alloys. *Adv Mater Res*, 2012, 418-420: 1346-1350.
- [8] Kandasamy J, Manzoor Hussain M, Rajesham S. Heterogeneous friction stir welding: improved properties in dissimilar aluminum alloy joints through insertion of copper coupled with external heating. *Mater Manuf Process*, 2012, 27: 1429-1436.
- [9] Sudeesh P, Sadeesh M, Venkatesh Kannan V, Rajkumar P, Avinash N, Arivazhagan K, Devendranath ramkumar K, Narayanan S. Studies on Friction Stir Welding of AA2024 and AA 6061 Dissimilar Metals. *Procedia Eng*, 2014, 75: 145-149.
- [10] Nik Z C, Ishak M, Othman N H. The Effect of Tool Pin Shape of Friction Stir Welding (FSW) on Polypropylene. *Mater Sci Eng*, 2017, 238: 012003
- [11] Weifeng Xu, Jinhe Liu, Hongqiang Zhu and Li Fu. Influence of welding parameters and tool pin profile on microstructure and mechanical properties along the thickness in a friction stir welded aluminium alloy. *Mater Des*, 2013, 47: 599-606.
- [12] Vijay SJ, Murugan N. Influence of tool pin profile on the metallurgical and mechanical properties of friction stir welded Al-10 wt.% TiB₂ metal matrix composite. *Mater Des*, 2010, 31: 3585-3589.
- [13] Morteza Ghaffarpour, Sina Kolahgar, Bijan Mollaei Dariani, Kamran Dehghani. Evaluation of dissimilar welds of 5083-H12 and 6061-T6 produced by friction stir welding. *Metall Mater Trans A*, 2013, 44A: 3697-3707.
- [14] Leitao B, Emillo BM, Chaparro DM, Rodrigues. Formability of similar and dissimilar friction stir welded AA5182-H111 and AA 6061-T4 tailored blanks. *Mater Des*, 2009, 30: 3235-3242.
- [15] Palanivel R, Koshy Mathews P. The tensile behaviour of friction-stir welded dissimilar aluminium alloy. *Mater Technol*, 2011, 45: 623-626.
- [16] Miles MP, Melton DW, Nelson TW. Formability of friction-stir-welded dissimilar-aluminium alloy sheets. *Metall Mater Trans A*, 2005, 36A: 3335-3342.
- [17] Padmanabhan R, Oliveira MC, Menezes LF. Deep drawing of aluminium-steel tailor-welded blanks. *Mater Des*, 2008, 29: 154-160.
- [18] Elangovan K, Balasubramanian V, Babu S. Predicting tensile strength of friction stir welded AA6061 aluminium alloy joints by a mathematical model. *Mater Des*, 2009, 30: 118-193.
- [19] Biswaijit Parida, Sukhomay Pal, Pankaj Biswas, Mohapatra MM, Sujoy Tikader. Mechanical and micro-structural study of FSW of aluminium alloys. *Int J Appl Res in Mech Eng*, 2011: 1.
- [20] Adel Mahmood Hassan, Tarek Qasim, Ahmed Ghaithan. Effect of pin profile on friction stir welded aluminium matrix composites. *Mater Manuf Process*, 2012, 27: 1397-1401.
- [21] Venkateswarlu G, Davidson MJ, Tagore GRN. Modelling studies of sheet metal formability of friction stir processed Mg AZ31B alloy under stretch forming. *Mater Des*, 2012, 40: 1-6.
- [22] Kang DH, Kim DW, Bae GT, Kim KH, Nack J Kim. Relationship between stretch formability and work-hardening capacity of twin-roll cast Mg alloys at room temperature. *Scripta Mater* 2009, 61: 768-771.
- [23] Kang DH, Kim DW, Kim S, Bae GT, Kim KH, Kim NJ. Room temperature formability of Mg alloys. *Mater Sci Forum*, 2009, 618-619: 463-466.
- [24] Lakshminarayanan AK, Balasubramanian V, Elangovan K. Effect of welding processes on tensile properties of AA6061 aluminium alloy joints. *Int J Adv Manuf Technol*, 2009, 40: 286-296.
- [25] Mouloud Aissani, Saliha Gachi, Fouad Boubenider, Younes Benkedda. Design and optimization of friction stir welding tool. *Mater Manuf Process*, 2010, 25: 1199-1205.



ARTICLE

Study on the Crystal Structure and Microstructure Evolution of Shock-processed Titanium Powder

A.D. Sharma* A.K. Sharma N.Thakur

1. Department of Physics, Government College Chowari, Chamba, 176302, India
2. Dean Research, Om Sterling University, Hisar -125001, India
3. Department of Physics, Himachal Pradesh University, Shimla, 171005, India

ARTICLE INFO

Article history

Received: 15 April 2019

Accepted: 22 October 2019

Published Online: 31 October 2019

Keywords:

Crystal structure

Microstructure

Shock waves

Rapid solidification

Titanium

ABSTRACT

Titanium powder was rapidly solidified by using shock-wave consolidation technique. The critical parameters were controlled by instrumented detonics and pin-oscillography. The compacted specimens were investigated for crystal structure and microstructural strengthening by using standard diagnostic techniques. The density of the final product was found to be greater than 96% of the theoretical value. X-ray diffraction pattern reveals intact crystalline structure without the presence of any undesired phases. The particle size reduction indicated by XRD was supported by laser diffraction based particle size analyzer. Results from energy dispersive spectroscopy ruled out the possibility of any segregation within the compacts. Scanning electron microscopy showed crack-free, voids-free, melt-free, fracture-less compacts of titanium with a unidirectional dendrite orientation without any grain-growth.

1. Introduction

Titanium has a moderate strength to weight ratio, corrosion resistant properties and ability to withstand at elevated temperature without creeping and thereby making it a strong candidate to be serviceable in modest aerospace industry, lightweight engine shafts, motor parts and making critical components for strategic cryogenic applications in defence^[1,2]. Several powder consolidation processes can be adopted to obtain an extensive range of rapidly solidified (RS) compositions of titanium. Rapid solidification can affect the resulting crystal structure, microstructure, morphology, constitution and mechanical properties of the specimen. Conventional compaction methods applied in powder metallurgy exert high pressure and temperature

on the specimen for long duration^[3]. This prolonged temperature exposure may result into grain-growth, melting of the compacted specimen and deteriorate the fine-grained structure that can reduce the mechanical properties.

As such the consolidation temperature must act relatively for lesser time. Therefore, innovative technique like shock wave compaction (SWC) has been developed. SWC is an emerging technology wherein fine powders are dynamically compressed to produce monoliths of desired dimensions. Shock wave being transient in nature requires no additional binders. With a working time of few micro-second, it offers opportunity to consolidate the fine powder particles without any grain-growth. The dynamic high pressure of shock wave causes pore-elim-

*Corresponding Author:

A.D. Sharma,

Department of Physics, Government College Chowari, Chamba, 176302, India;

Email: ads.hpu@gmail.com

ination whereas the transient high temperature leads to surface heating, resulting into interfacial locking of the particles while keeping the particle interior intact from high temperature exposure [4]. Figure 1 represents different processes ongoing during the SWC of powders. The present study aims at producing compacted specimen of pure titanium powder under shock-wave loading while retaining its crystal structure without formation of undesired phases and obtaining a better microstructure without grain-growth, without melting or without segregation. The objective is to correlate theoretical considerations with experimental analysis as well.

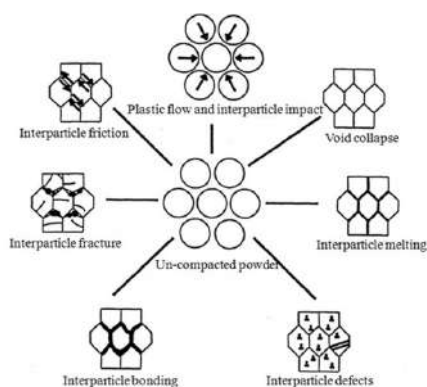


Figure 1. Various modes of energy dissipation in SWC of powders

2. Experimental Work

The experimental work comprises two parts: one involves the compaction phenomenon and the other concentrates on the analysis of the specimen using standard diagnostic techniques. Figure 2 represents a block diagram of the SWC system. It consists of a cylindrical ampoule with a conical cap at top and a plane cap in the bottom of the cylinder. Titanium powder is filled in this cylindrical ampoule with special care that air may not remain entrapped between the fine-grained particles. This cylindrical geometry is now put inside a perplex pipe filled gently with an explosive material. A detonator covers the top of the specimen-loaded arrangement. A pin oscillographic technique including a pulse generator (pulser) and a Digital Storage Oscilloscope (DSO) was used to measure velocity of detonation. The choice of explosive is very critical aspect for SWC as it involves detonation wave, shock wave and expanding gases that may directly affect the corresponding microstructure of the specimen under consideration. An explosive called trimonite with a moderate velocity of detonation is used for this specific purpose. The whole configuration placed in an earth pit is detonated with the help of exploder dynamo condenser (EDC). The detonation

wave on combination with explosive produces a spherical shock-front that swiftly travels down to the compaction system. The spherical shock-front becomes plane wave-front after passing through the conical top. This planer shock-front travels gradually down to the ampule and is responsible for the compaction of the powder [5].

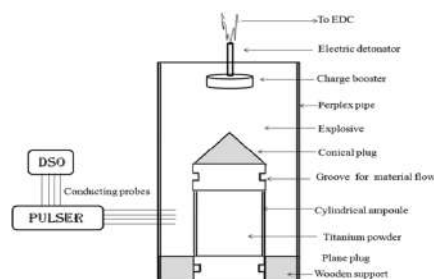


Figure 2. Compaction geometry for SWC of titanium powder

X-ray diffraction (XRD) technique was employed to determine the crystal structure, phase and FWHM values. The device used was X'PERT-PRO X-ray detector with a fixed divergence slit operating at 45kV and 40mA, with a step-time of 1.0s and step-angle 0.02° using Cu K_α lines having wavelength of the order of 1.54\AA . The goniometer was varied through the angle (2θ) from 10° to 80° . The variation in particle size of the shock-processed specimen was examined with the help of laser diffraction based particle size analyzer (Malvern mastersizer, S-2000) having lens range 300RF and a beam length of 1.9mm working at wavelength of 633nm. The chemical homogeneity and segregation within the compacted specimen were examined by using energy dispersive spectroscopy (EDS, Genesis APEX4) with a single shot multibox detector, SSD Apollo10, at energy ranging from 0-30 keV. To determine the surface morphology, core microstructure, melting, fractures and cracking of the shock-processed specimen, scanning electron microscopy, (SEM) FEI, Quanta 250, D-9393 operating at 20 kV was used.

3. Results and Discussion

3.1 Determination of crystal structure and phases

Figure 3 represents graphic workspace fit X-ray diffraction pattern of un-processed and shock-processed titanium powder. XRD study reveals that the shock-processed titanium is much similar to the un-processed specimen. The diffraction peaks (001), (100), (101), (110), (102) and (111) confirm hcp crystal structure of titanium. After being indexed, the peak position of shock-processed specimen found to possess same crystalline phase as that of un-processed specimen. No extra peak was observed in the compacted specimen that rules out the possibility

of impurity and presence other phases. It can also be seen in the X-ray pattern that FWHM values of the shock-processed specimen have been increased significantly (from 0.4793 to 0.9507⁰2θ). One can conclude from the well-known Scherrer's formula that grain size has been reduced in the compacted specimen. This broadening in the diffraction peaks attributes to a decrease in crystallite size under intense shock-loading. The slight shift of the diffraction peaks towards the higher angle also point towards the decrease in lattice parameters (Bragg's law). This shift in peak position may be attributed to a few crystalline defects owing to the melting of particle interfaces^[6,7]. More intense peaks in the diffraction pattern of shock-processed specimen indicate the more density of the particles at that particular position or plane. A careful observation of the X-ray depicts that there is small disturbance or we may say small peaks around the 52⁰ and 64⁰(2θ) in the shock-processed specimen whereas no such disturbance/peak is observed in the pure titanium powder^[8]. These peaks point towards the oxide formation in the compacted specimen. The justification stems from the fact that air may remain entrapped during the tapping of the powder in the cylindrical ampoule resulting into oxide formation. Oxide formations in the compacts are responsible for lower density of the final product^[9,10].

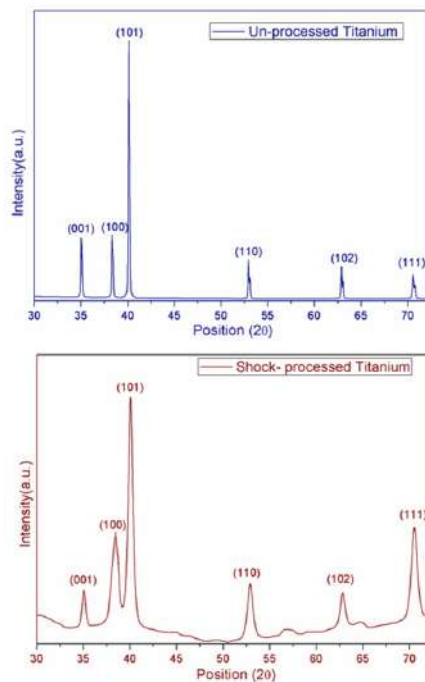


Figure 3. Graphic workspace fit XRD pattern for un-processed and shock- processed titanium

3.2 Determination of Particle Sizes

To support the reduction in particle size in the compacted

specimen revealed by the X-ray diffraction method, we used laser diffraction method. It applies small angle laser light scattering principle to measure particle size distributions of powder. Figure 4 shows Gaussian fit particle size distribution (logarithmically normal) for un-processed and shock-processed titanium. Table 1 represents the data recovered from laser diffraction method. D(v,0.9) reflects 90% of the sample is under this size. Similarly, D(v,0.1) means 10% of the sample is below this size and likewise D(v,0.5) denotes 50% of the particles lie below this size range. The volume moment mean diameter D(4,3) was calculated by using the relation: $\bar{D}_{(4,3)} = \frac{\sum V_i d_i^4}{\sum V_i d_i^3}$. Where, V_i is the volume of particles and d_i is actual surface area of the particles called de-Broncker mean diameter^[11].

The density of the shock-processed specimen found nearly the theoretical value (4.506g/cm³). That means SWC technique is quite helpful to achieve a density more than 96% of the actual value. For un-processed powder specimen, average moment mean diameter was found to be 32.56μm which had been reduced down to 24μm.

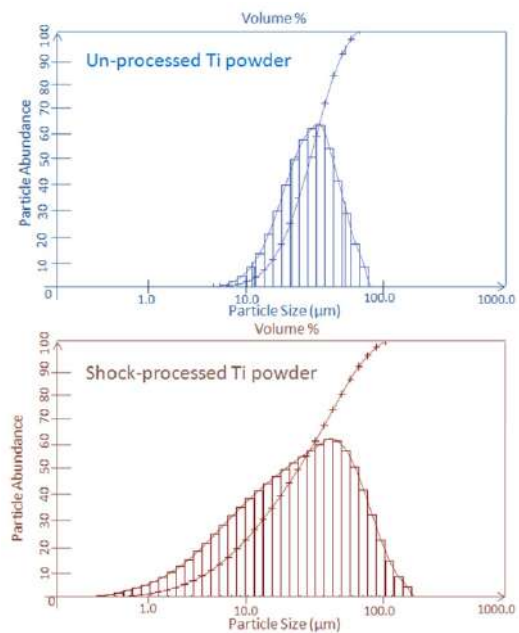


Figure 4. laser diffraction based particle size distribution for un-processed and shock-processed titanium

Table 1. Data recovered from laser diffraction on the pure and shock-processed titanium

Parameters	Un-processed Ti	Shock-Processed Ti
Specific Surface Area	0.1395m ² /g	0.0586 m ² /g
D [v,0.9]	48.06 μm	40.25 μm
D [v,0.1]	10.80 μm	12.40 μm
D [v,0.5]	27.65 μm	24.35 μm
D [4, 3]	32.56 μm	24.03 μm

3.3 Determination of Elemental Composition and Segregation

There may arise some problems with respect to the segregation of impurity elements and coarse inter-metallic compounds due to the formation of new phases in SWC process. Better microstructure controls the segregation phenomenon and dispersed position of non-metallic inclusions. Therefore, energy dispersive spectroscopy is used to explore compositional changes and segregation within the compacted specimen.

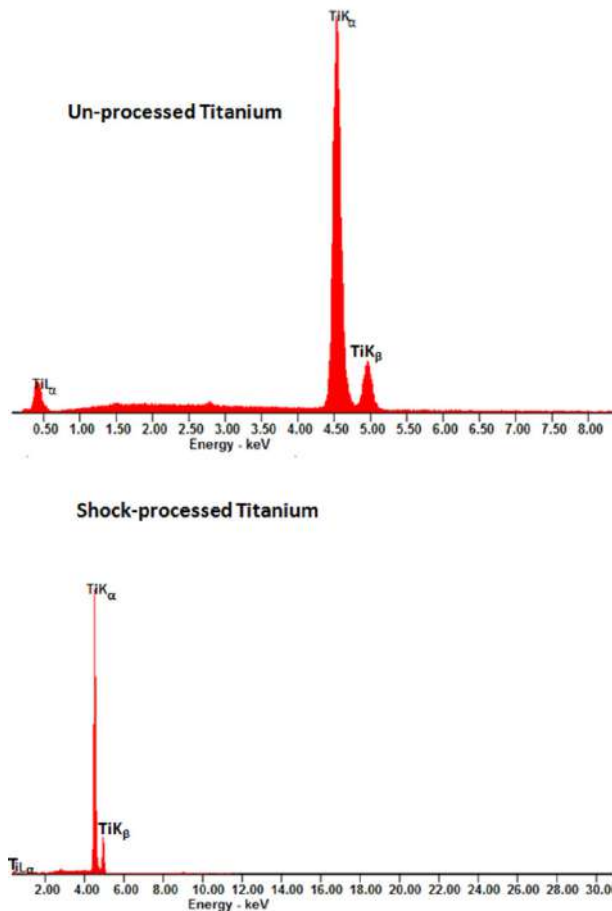


Figure 5. EDX data indicating no segregation within the compacted specimen

Figure 5 shows the energy dispersive spectra of pure titanium (99.96% purity) and shock-processed Titanium. Quantitative EDX data suggested no segregation within the compacts after the shock-loading. In fact, the sample under investigation was put into large energy range upto 30keV but only three peaks TiK_{α} , TiK_{β} and TiL_{α} were observed with the same peak positions. This means that the sample possess chemical homogeneity. Since, the rapid solidification occurs at quench rates of the order of 10^5 K/s for particles of $100\mu\text{m}$ or less^[12]. This high-quenching during rapid solidification minimize chemical segregation

and formation of massive phases and hence ensures a homogeneous fine-grained structure.

3.4 Determination of Morphology and Microstructure Evolution

Figure 6(a) is an SEM picture of pure titanium powder. The particles are primarily of various sizes and morphologies. The particles are rough needlelike structure. Some particles appeared to be crystalline while others appeared amorphous. Even after size classification, large variations in particle morphology and structure were observed. The particle-size of the titanium powder calculated from SEM image found to be $\sim 30\mu\text{m}$ that supports the earlier observation. Figure 6(b) concentrates on a single particle at a higher magnification ($4000\times$). The morphology of the particle consists of uneven smooth surface. It reflects distribution fine dendritic structure on the surface of particle in different directions. Such irregularities are favorable for SWC as it may produce better interlocking between particles and lead to higher density of the final product.

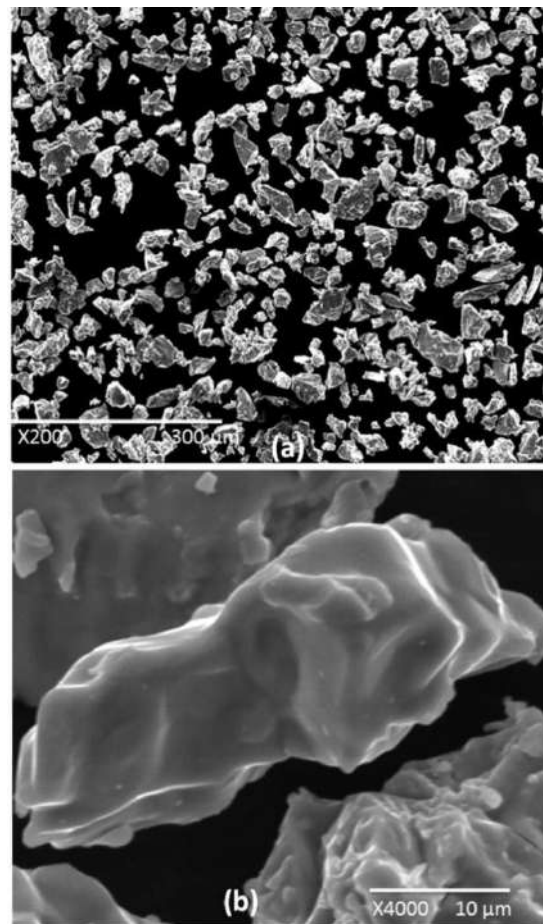


Figure 6 (a). SEM image of pure titanium powder particles. (b) magnified image of a single particle showing its surface morphology

Working with shock-loading of metal powders faces a major problem with melting of the final product. Therefore, micrograph images were taken from the inner portion of the shock-processed specimen at different magnifications to realize these issues. Figure 7(a) and (b) demonstrate core fracture morphology of the shock-processed titanium with unidirectional heat-flow. It can be seen from higher magnified image that dendrites are oriented in the direction of heat-flow within the compacts. Such structure supposed to possess good mechanical properties. Distinctive grain boundary can be seen at higher magnification (1200×). Two sub-structurally different regions can also be observed in figure 7(c) and (d), respectively. Regions marked with “A” showing only little cracking of the compacts. Cracking may be due to uneven load under deliberate breaking of the compacts to observe these regions within the core of compacted titanium. Cracking within the compacted specimen is attributed to tensile/compressive stresses, and shear instability or solidification shrinkage.

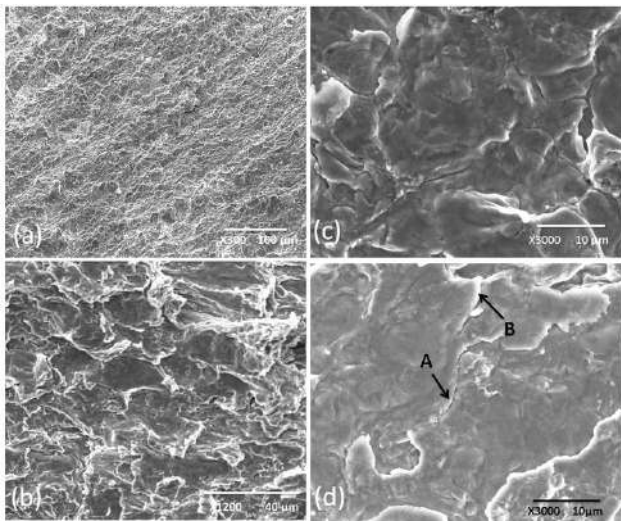


Figure 7 (a). heat-flow throughout the surface of compacted specimen. (b) higher magnified image showing dendrite orientation within the inner portions of compacts. (c) fractograph showing the well-bonded structure in the core of compacted specimen surface (d) microstructure across the grain boundaries

No micro-void was observed in the whole compacted specimen. The regions marked with ‘B’ correspond to melting across particle interfacial. These melting layers are responsible for the bonding between the particles under the intense deposition of shock-energy. Because shock pulses being transient in nature apply only for few micro-seconds, the melted layers re-solidify instantly and the grains do not respond against their growth during SWC process. Thus, the apparent white regions across the

grain boundaries are produced due to rapid- solidification shrinkage^[13]. The grains of the shock-processed specimen seem to be of smaller size as that of un-processed specimen shown by figure 7(d). It is clear that shock wave loading considerably deformed the particle shapes as well. These irregularities increase the contact area of the specimen and hence the strength considerably. Such sub-structurally unique situations under controlled parameters lead to better microstructures that provide better end products^[14].

4. Conclusions

SWC technique helped in forming the uniform melt-free, crack-free, voids-free compacts of titanium powder. The crystalline structure of the compacted specimen remained intact. No impurity or phase of any other kind was detected. There is no segregation within the compacts. A remarkable particle size reduction was observed that rules out the possibility of grain-growth during compaction process. The density of the final product was found to be more than 96% of the theoretical value. Shock-wave consolidation being transient in nature, owing to its short processing time, controlled parameters and high quench-rates proven to be a very helpful technique for obtaining a stable structural and microstructural products.

Acknowledgements

The corresponding author wishes to thank Dr. Ashok Kumar Sharma, Retired Senior Scientist from Defence Research and Development Organization of India for his keen concern and enthusiastic approach during the trial process. Thanks is also due to the Professor Nagesh Thakur, H.P. University, for his reasoned guidance and critical discussion throughout the work.

References

- [1] Metals Handbook, 1980, 3.
- [2] ASM Handbook, 1990, 1.
- [3] C. Suryanarayana, F.R. Froes, The current status of titanium rapid solidification, Journal of the Minerals, Metals & Materials Society, 1990, 1: 22-25.
- [4] A.D. Sharma, A.K. Sharma, N. Thakur, Crystallographic, microstructural and mechanical characterization of dynamically- processed EP741NP superalloy, J. Metall. and Material. Trans. B; 2016, 47: 2479-2486.
- [5] M.A. Meyers, Dynamic Behavior of Materials. Wiley Pub. New York, 1994.
- [6] Komizoyu-ichi, Terasaki Hidenori, Saiki Keta, Ideka Masahiko, Direct observation of solidification and

- phase transformation in pure titanium, *Transaction of JWRI*, 2009, 38: 43-47.
- [7] A. A. Bukaemskii and E.N. Fedorova, Explosive compaction and low-temperature sintering of alumina nano-powders, *Combust. Explos. Shock Waves.*, 2008, 44(6): 717-728.
- [8] I.M. Meléndez, C. Arévalo, E. M. P. Soriano, M. Kitzmantel, E. Neubauer, Microstructural and XRD Analysis and Study of the Properties of the System Ti-TiAl-B4C Processed under Different Operational Conditions, *Metals*, MDPI, 2018, 8: 367-382.
- [9] T. Thotsaphone, K. Katsuyoshi, I. Hisashi, U. Junko, F. Bunshi. Microstrure and mechanical properties of powder metallurgy pure titanium composite reinforced with carbon nanotubes. *Trans. JWRI*, 2008, 37(1): 57-61.
- [10] A.D. Sharma, A.K. Sharma, N. Thakur, Crystallographic and morphological characteristics of explosively compacted copper under various detonation velocities, *Phil. Mag.*, 2012, 92(16): 2108-2116.
- [11] A.D. Sharma, A.K. Sharma, N. Thakur, Crystallographic, microstructure and mechanical characteristics of dynamically processed IN718 superalloy, *J. Alloy. Comp.* 2014, 597: 175–180.
- [12] C.T. Wei, E. Vitali, F. Jiang; S.W. Du, D.J. Benson, K.S. Vecchio, N.N. Thadhani, M.A. Meyers, Quasi-static and dynamic response of explosively consolidated metal- aluminum powder mixtures, *Acta mater.* 2012, 60(2): 1418-1432.
- [13] W. Salas, N. Alba- baena, L.Murr, Explosive Shock-Wave Consolidation of Aluminum Powder/Carbon Nanotube Aggregate Mixtures: Optical and Electron Metallography, *metal. Mater. Trans. A*, 2007, 38(12): 2928-2935.
- [14] A.D. Sharma, A.K. Sharma, N. Thakur, Effect of explosive contact and non-contact processing on structure, microstructure and mechanical characteristics of aluminium., 2013, 111(3): 783-789.

Author Guidelines

This document provides some guidelines to authors for submission in order to work towards a seamless submission process. While complete adherence to the following guidelines is not enforced, authors should note that following through with the guidelines will be helpful in expediting the copyediting and proofreading processes, and allow for improved readability during the review process.

I . Format

- Program: Microsoft Word (preferred)
- Font: Times New Roman
- Size: 12
- Style: Normal
- Paragraph: Justified
- Required Documents

II . Cover Letter

All articles should include a cover letter as a separate document.

The cover letter should include:

- Names and affiliation of author(s)

The corresponding author should be identified.

Eg. Department, University, Province/City/State, Postal Code, Country

- A brief description of the novelty and importance of the findings detailed in the paper

Declaration

v Conflict of Interest

Examples of conflicts of interest include (but are not limited to):

- Research grants
- Honoria
- Employment or consultation
- Project sponsors
- Author's position on advisory boards or board of directors/management relationships
- Multiple affiliation
- Other financial relationships/support
- Informed Consent

This section confirms that written consent was obtained from all participants prior to the study.

- Ethical Approval

Eg. The paper received the ethical approval of XXX Ethics Committee.

- Trial Registration

Eg. Name of Trial Registry: Trial Registration Number

- Contributorship

The role(s) that each author undertook should be reflected in this section. This section affirms that each credited author has had a significant contribution to the article.

1. Main Manuscript

2. Reference List

3. Supplementary Data/Information

Supplementary figures, small tables, text etc.

As supplementary data/information is not copyedited/proofread, kindly ensure that the section is free from errors, and is presented clearly.

III. Abstract

A general introduction to the research topic of the paper should be provided, along with a brief summary of its main results and implications. Kindly ensure the abstract is self-contained and remains readable to a wider audience. The abstract should also be kept to a maximum of 200 words.

Authors should also include 5-8 keywords after the abstract, separated by a semi-colon, avoiding the words already used in the title of the article.

Abstract and keywords should be reflected as font size 14.

IV. Title

The title should not exceed 50 words. Authors are encouraged to keep their titles succinct and relevant.

Titles should be reflected as font size 26, and in bold type.

IV. Section Headings

Section headings, sub-headings, and sub-subheadings should be differentiated by font size.

Section Headings: Font size 22, bold type

Sub-Headings: Font size 16, bold type

Sub-Subheadings: Font size 14, bold type

Main Manuscript Outline

V. Introduction

The introduction should highlight the significance of the research conducted, in particular, in relation to current state of research in the field. A clear research objective should be conveyed within a single sentence.

VI. Methodology/Methods

In this section, the methods used to obtain the results in the paper should be clearly elucidated. This allows readers to be able to replicate the study in the future. Authors should ensure that any references made to other research or experiments should be clearly cited.

VII. Results

In this section, the results of experiments conducted should be detailed. The results should not be discussed at length in

this section. Alternatively, Results and Discussion can also be combined to a single section.

VIII. Discussion

In this section, the results of the experiments conducted can be discussed in detail. Authors should discuss the direct and indirect implications of their findings, and also discuss if the results obtain reflect the current state of research in the field. Applications for the research should be discussed in this section. Suggestions for future research can also be discussed in this section.

IX. Conclusion

This section offers closure for the paper. An effective conclusion will need to sum up the principal findings of the papers, and its implications for further research.

X. References

References should be included as a separate page from the main manuscript. For parts of the manuscript that have referenced a particular source, a superscript (ie. [x]) should be included next to the referenced text.

[x] refers to the allocated number of the source under the Reference List (eg. [1], [2], [3])

In the References section, the corresponding source should be referenced as:

[x] Author(s). Article Title [Publication Type]. Journal Name, Vol. No., Issue No.: Page numbers. (DOI number)

XI. Glossary of Publication Type

J = Journal/Magazine

M = Monograph/Book

C = (Article) Collection

D = Dissertation/Thesis

P = Patent

S = Standards

N = Newspapers

R = Reports

Kindly note that the order of appearance of the referenced source should follow its order of appearance in the main manuscript.

Graphs, Figures, Tables, and Equations

Graphs, figures and tables should be labelled closely below it and aligned to the center. Each data presentation type should be labelled as Graph, Figure, or Table, and its sequence should be in running order, separate from each other.

Equations should be aligned to the left, and numbered with in running order with its number in parenthesis (aligned right).

XII. Others

Conflicts of interest, acknowledgements, and publication ethics should also be declared in the final version of the manuscript. Instructions have been provided as its counterpart under Cover Letter.

About the Publisher

Bilingual Publishing Co. (BPC) is an international publisher of online, open access and scholarly peer-reviewed journals covering a wide range of academic disciplines including science, technology, medicine, engineering, education and social science. Reflecting the latest research from a broad sweep of subjects, our content is accessible world-wide—both in print and online.

BPC aims to provide an analytics as well as platform for information exchange and discussion that help organizations and professionals in advancing society for the betterment of mankind. BPC hopes to be indexed by well-known databases in order to expand its reach to the science community, and eventually grow to be a reputable publisher recognized by scholars and researchers around the world.

BPC adopts the Open Journal Systems, see on ojs.bilpublishing.com

Database Inclusion



Asia & Pacific Science
Citation Index



Creative Commons



China National Knowledge
Infrastructure



Google Scholar

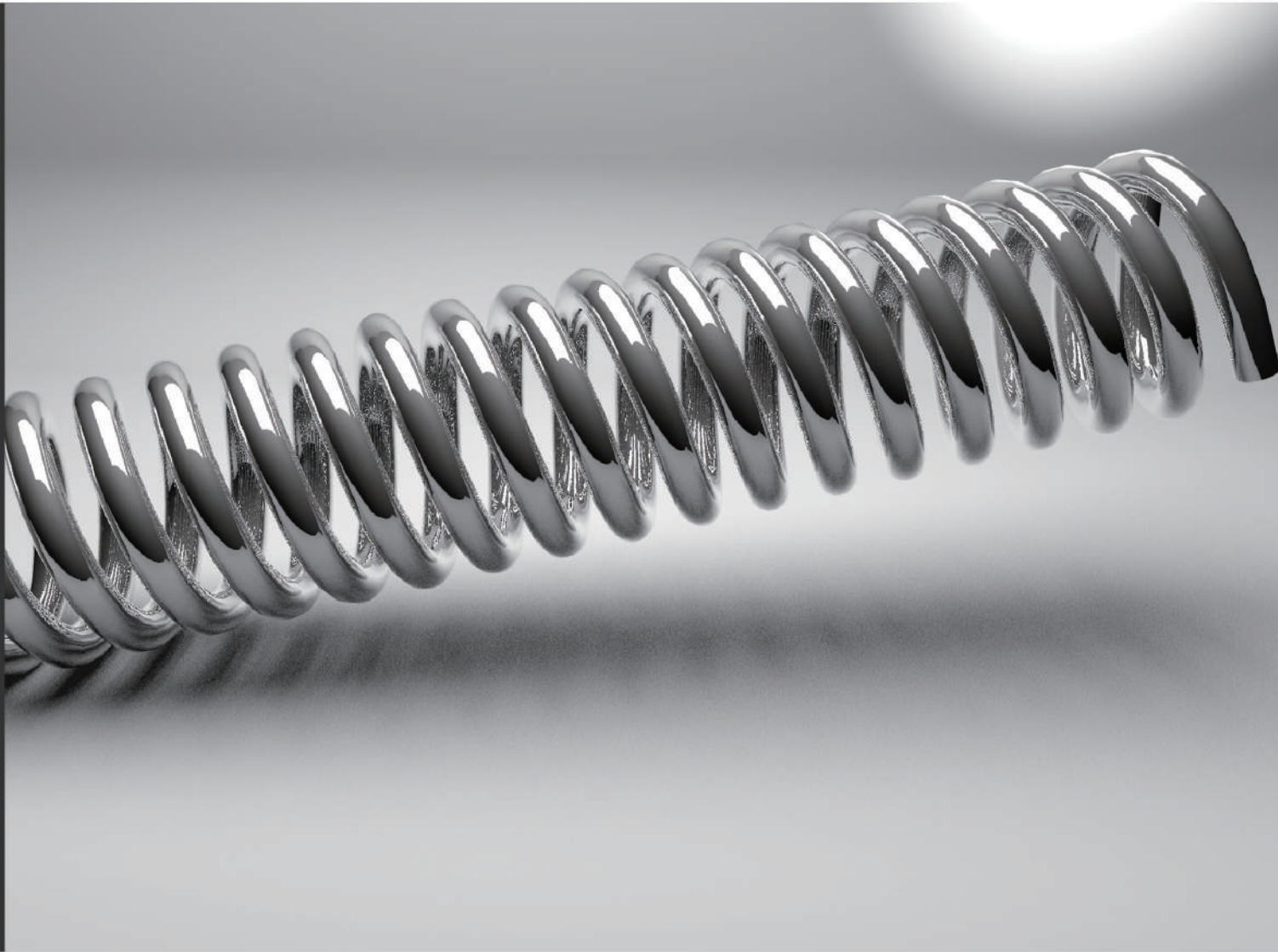


Crossref



MyScienceWork

Bilingual Publishing Co. is a company registered in Singapore in 1984, whose office is at 12 Eu Tong Sen Street, #08-169, Singapore 059819, enjoying a high reputation in Southeast Asian countries, even around the world.



Tel: +65 65881289
E-mail: contact@bilpublishing.com
Website: www.bilpublishing.com



**BILINGUAL
PUBLISHING CO.**
Pioneer of Global Academics Since 1984

ISSN 2630-5135



9 772630 513199